Nanoscale

PAPER

View Article Online
View Journal | View Issue

Cite this: *Nanoscale*, 2023, **15**, 12748

Anti-amyloidogenic amphipathic arginine-dehydrophenylalanine spheres capped selenium nanoparticles as potent therapeutic moieties for Alzheimer's disease†

Avneet Kour,[a,b] Virendra Tiwari,[c] Nidhi Aggarwal,[a] Himanshu Sekhar Panda,[a] Ashwani Kumar,[b] Siddharth Tiwari,[d] Virander Singh Chauhan,[e] Shubha Shukla*[c] and Jiban Jyoti Panda *[a]

Aggregation of both amyloid beta (Aβ) peptide and hyperphosphorylated tau proteins is the major pathological hallmark of Alzheimer's disease (AD). Moieties that carry anti-amyloidogenic potency against both of the aggregating entities are considered to be promising drug candidatures for the disease. In the current work, we have synthesized amphipathic dipeptide vesicle-templated selenium nanoparticles (RΔF-SeNPs) as potential entities to combat AD. We have investigated and established their anti-amyloidogenic activity against different peptide-based amyloid models, such as the reductionist model based on the dipeptide phenylalanine–phenylalanine (FF) derived from Aβ; a model based on the hexapeptide Ac-PHF6 (^{306}VQIVYK^{311}) derived from tau protein; and the full-length Aβ42 polypeptide-based model. We also evaluated the neuroprotective characteristics of RΔF-SeNPs against FF, Ac-PHF6, and Aβ42 fibril-induced toxicity in neuroblastoma, SH-SY5Y cells. RΔF-SeNPs further exhibited neuroprotective effects in streptozotocin (STZ) treated neuronal (N2a) cells carrying AD-like features. In addition, studies conducted in an intra-cerebroventricular STZ-instigated rat model of dementia revealed that RΔF-SeNP-treated animals showed improved cognitive activity and reduced Aβ42 aggregate burden in brain tissues as compared with the STZ-treated group. Moreover, *in vivo* brain distribution studies conducted in animal models additionally demonstrated the brain-homing ability of RΔF-SeNPs. All together, these studies supported the potency of RΔF-SeNPs as efficient and propitious disease-modifying therapeutic agents for combating AD.

Received 4th April 2023,
Accepted 21st June 2023

DOI: 10.1039/d3nr01558k

rsc.li/nanoscale

1. Introduction

Alzheimer's disease (AD) is a protein/peptide misfolding neurological disorder and is one of the prominent types of dementia.[1] It is manifested by impairments in several cognitive functions including memory, language, and visuospatial activities, which lead to a loss of the patient's ability to perform daily chores.[2] After heart disease, cancer, and brain stroke, AD is the fourth leading cause of mortality. Up until 2022, AD had affected over 6.5 million Americans aged around 65 and above. This figure may rise to 13.8 million by 2060 if suitable medical breakthroughs are not developed to prevent, hinder or cure AD.[3]

The foremost neuropathological insignias of AD are the generation of extracellular amyloid aggregates and intracellular neurofibrillary tangles derived from amyloid β peptides (Aβ) and the hyperphosphorylated tau protein, respectively.[4] Therefore, targeting and abrogating the aggregation of both Aβ as well as tau protein simultaneously could be an effective and viable approach for the efficient treatment of AD. Selenium (Se) is an important minor trace element with low toxicity and with various physiological functions including anti-oxidation and immune regulation.[5] In the human body, the metal forms a major component of the structural framework of twenty-five selenoproteins that includes thioredoxin reductase, glutathione peroxidase (GPx), and glutathione hydroxyl peroxidase. These proteins maintain the metabolic rate of neurotransmit-

[a]*Institute of Nano Science and Technology, Mohali, Punjab 140306, India. E-mail: jyoti@inst.ac.in*
[b]*University Institute of Pharmaceutical Sciences, Punjab University, Chandigarh 160014, India*
[c]*CSIR-Central Drug Research Institute, Sector 10, Jankipuram Extension, Sitapur Road, Lucknow 226031, India. E-mail: shubha_shukla@cdri.res.in*
[d]*National Agri-Food Biotechnology Institute (NABI), Mohali, Punjab 140308, India*
[e]*International Centre for Genetic Engineering and Biotechnology, New Delhi 110067, India*

† Electronic supplementary information (ESI) available. See DOI: https://doi.org/10.1039/d3nr01558k

ters, regulate the secretion of hormones, and antagonize heavy metal-induced aggregation.[6–8] Low levels of bodily Se are associated with cognitive impairment, depression, and anxiety.[9] Se is shown to be engaged in AD prevention owing to its excellent antioxidant and neuroprotective properties. It has the ability to ameliorate the pathophysiological symptoms of various neurodegenerative diseases.[10] It can attenuate Aβ deposition as well as tau protein hyperphosphorylation, major factors involved in AD progression.[11] Se can form nanoparticulate structures (SeNPs) and these nanoforms of the metal exhibit excellent antioxidant properties.[12] SeNPs are generally fabricated following various methods including physical[13] and chemical procedures,[14] or following green synthesis procedures.[15] These have been explored as various therapeutic modalities such as antiviral candidates against the H1N1 influenza virus,[16] antidiabetic agents,[17] antimicrobial agents,[18] anticancer agents,[19] and candidates for targeted stroke therapy.[20] In recent years, SeNPs have been employed as therapeutic entities for the treatment of numerous neurological maladies.[21] SeNPs have also been widely explored as a therapeutic moiety for the treatment of AD. A multifunctional selenium-polydopamine nanozyme (Se@PDA@Bor) developed by Gong *et al.* has been shown to relieve neuroinflammation, decrease Aβ burden, and improve memory in APP/PS1 transgenic AD mice.[22] In another report, mesoporous nano-selenium (MSe) inhibited the agglomeration of Aβ protein, reduced oxidative stress, reduced tau hyperphosphorylation, prevented nerve cell damage and improved memory impairment in APP/PS1 mice.[23] Sialic acid-modified SeNPs conjugated with the peptide-B6 (B6-SA-SeNPs) exhibited high permeability across the BBB and further inhibited as well as disaggregated Aβ fibrils in AD.[24] In another study, SeNPs were coated with dihydromyricetin (DMY) to form DMY@SeNPs and with chitosan to form CS/DMY@SeNPs. These were further decorated with the BBB-targeting peptide Tg (TGNYKALHPHNG), to form Tg-CS/DMY@SeNPs, which diminished the aggregation of Aβ and helped in tackling neuroinflammation, aiding in AD therapy.[25] However, the efficient transport of SeNPs to the neuronal tissues for the treatment of AD is limited due to their incompetence in bypassing the blood–brain barrier (BBB).[26] The BBB is an arduous brain-specific gatekeeper that blocks the transit of drugs into the brain tissues.[27] Thus, it acts as a roadblock for the successful brain drug delivery of many potent neural therapeutic modalities and hinders the efficacy of many therapies aimed at AD cure. To address this problem, here we have utilized an amphipathic dipeptide, arginine-dehydrophenylalanine (RΔF) derived nanospheres, as capping entities for the pre-synthesized SeNPs. This coating enabled the non-invasive administration of SeNPs into brain tissues.

The predisposition of full-length proteins to self-assemble under *in vivo* conditions often generates poor, non-reproducible biophysical and biological results.[28] Therefore, the utility of short amyloidogenic peptide-based models to screen potential anti-amyloid therapeutics has gained importance and also significantly revolutionized the comprehension of overall amyloid production mechanisms. Some of these models are based on peptides which include the hexapeptide NFGAIL, derivative from islet amyloid polypeptide,[29] the pentapeptide DFNKF, derived from calcitonin,[30] and the heptapeptide KLVFFAE, derived from Aβ.[31] These short amyloid peptide sequences have been exemplified to encompass all the necessary molecular as well as structural information required for the generation of amyloid fibrils.[32] Gazit *et al.* reported that the diphenylalanine (FF) residue placed at locations 19 and 20 of the Aβ protein sequence contributes significantly towards mediating the preliminary sequence of interactions among the peptide monomers to trigger self-assembly and the subsequent formation of amyloid-associated fibrils.[33] In our recent work, we also corroborated the usage of dipeptide-FF based models for the screening of potent anti-amyloidogenic nano moieties.[34] Similarly, tau protein aggregation has been shown to be mediated by the self-assembly of a highly aggregative short peptide sequence, ^{306}VQIVYK^{311} (PHF6), situated in the third repeat of the microtubule-binding region.[35,36] This hexapeptide is responsible for mediating the oligomerization of the neurotoxic protein tau, and has been extensively utilized as a model system for evaluating the tau aggregation process and screening potent anti-amyloidogenic candidates.[37,38]

Thus, in this report, we explored the anti-amyloidogenic activity of RΔF-SeNPs towards both FF and Ac-PHF6-based amyloid aggregation models. The anti-amyloidogenic activity of RΔF-SeNPs was also assessed against the full-length Aβ42 peptide-based aggregation model.

Streptozotocin (STZ) administered by intracerebroventricular (ICV) injection in rat brains causes oxidative stress and finally induces AD.[39] STZ cytotoxicity has also been assessed in various neural cell types to understand different cellular processes that are accountable for mediating cell death in AD. As reported earlier, STZ-exposed neuronal cells (N2a) were used as an *in vitro* experimental test model for AD.[40,41] Hence, we next tried to explore the anti-amyloidogenic potential of our NPs towards STZ-treated N2a cells expressing amyloidogenic traits. These NPs may serve as excellent templates for the design and fabrication of efficient anti-amyloid nanotherapeutics (Scheme 1).

2. Experimental section

2.1. Materials

N-Methyl morpholine, sodium selenite, sodium chloride, L-phenylalanine, tetrahydrofuran, acetic anhydride, ascorbic acid, sodium hydroxide, isobutyl chloroformate, Boc-Phe-OH, sodium bicarbonate, sodium sulfate, sodium acetate, citric acid, 3-(4,5-dimethyl-thiazolyl)-2,5-diphenyltetrazolium bromide (MTT) and indocyanine green (ICG) were purchased from Sisco Research Laboratories, TCI Chemicals and HiMedia Laboratories Pvt. Ltd, India. 1,1,1,3,3,3-Hexafluro-2-propanol (HFIP), thioflavin T (ThT), rhodamine 6G, Aβ42 peptide, 4′-dianilino-1,1′-binaphthyl-5,5′-disulfonic acid dipotassium salt (Bis-ANS), methanol, 4′,6-diamidino-2-phenylindole (DAPI),

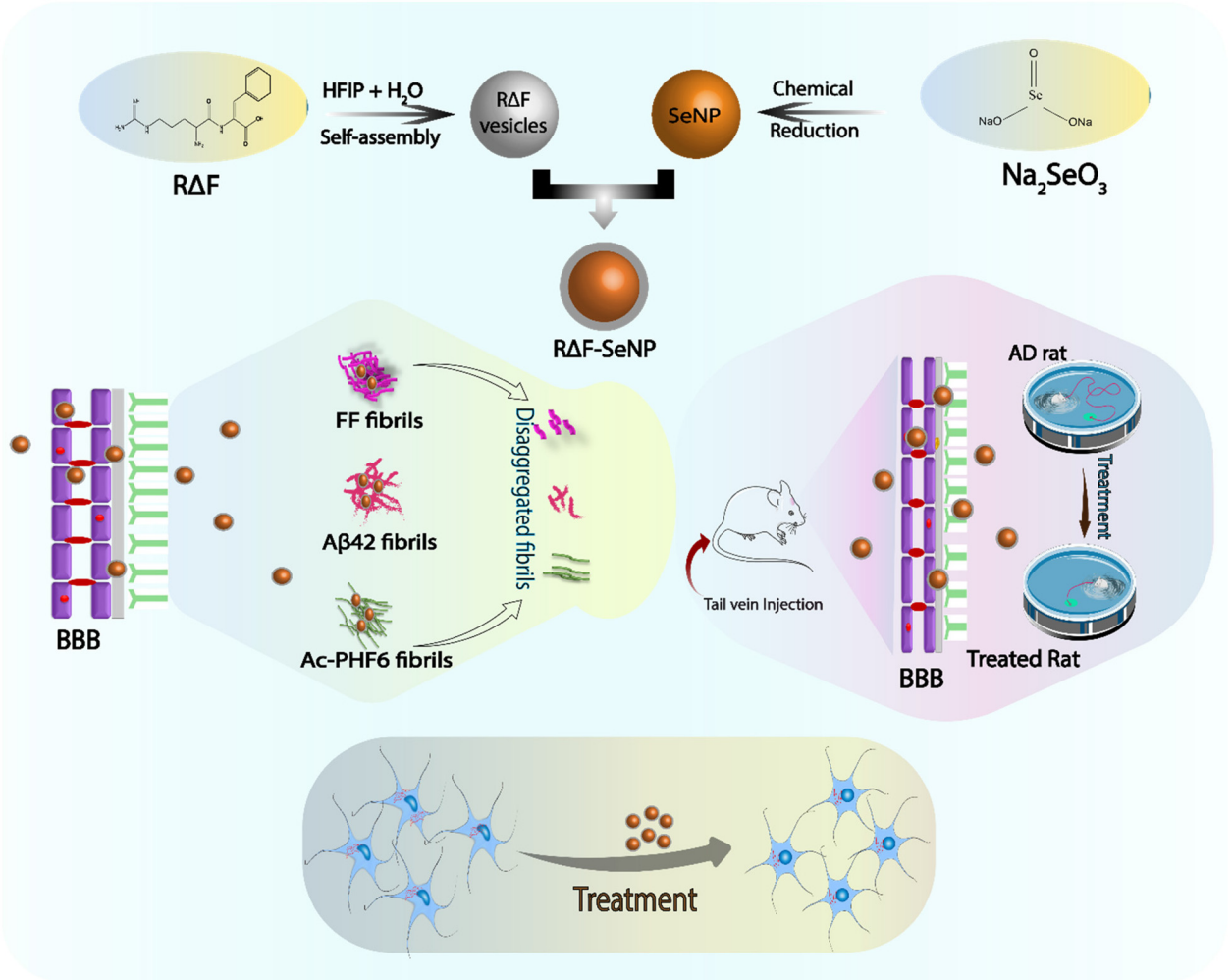

Scheme 1 Depicting the fabrication of RΔF nanosphere-capped SeNPs along with the exhibition of their anti-amyloidogenic activity towards FF, Ac-PHF6, and Aβ42 aggregates. It also demonstrates the ability of RΔF-SeNPs to cross the BBB. Furthermore, the protective effect exhibited by RΔF-SeNPs against STZ-induced cytotoxicity in neuronal cells as well as the improvement of cognitive performance in STZ-induced rat AD models by the NPs have also been exemplified.

streptozotocin, and dichloromethane (DCM) were obtained from Sigma Aldrich, Munich, Germany. Pentobarbitone sodium was procured from Sigma-Aldrich (USA). Calcein AM, Dulbecco's modified Eagle's medium (DMEM/F12), propidium iodide (PI), fetal bovine serum (FBS), antibiotic antimycotic solution (100×), phosphate buffered saline (PBS), and trypsin EDTA solution (1×) were procured from Gibco and Thermo Fisher Scientific Inc., NY, USA. Anti-Aβ 1 : 500, from Novus, USA, and Alexa Fluor-488/494 secondary antibody were procured from Invitrogen, Carlsbad (USA).

2.2. Synthesis of model amyloid peptides, FF and Ac-VQIVYK-NH_2, and the dipeptide RΔF

Diphenylalanine (FF) was synthesized by using the classical solution-phase peptide synthesis method as reported previously.[42,43] Ac-PHF6 (Ac-VQIVYK-NH_2) was synthesized by using a Liberty Blue CEM microwave automated peptide synthesizer (Matthews, NC, USA) as explained in ESI S1.† The dipeptide RΔF was synthesized *via* solution-phase peptide synthesis as described previously.[42,44] The synthesized peptides were characterized using HPLC or mass spectrometry.

2.3. Synthesis of RΔF vesicle-capped SeNPs

RΔF NPs were synthesized by following the procedure of molecular self-assembly. In brief, RΔF (1 mg) was dispersed in HFIP (50 μL) followed by dilution in water (950 μL) for initiating the self-assembly process. The formed particulate suspension was further incubated for 1 hour (h) at room temperature (RT) to generate a stable assembly. The synthesis of SeNPs was achieved using sodium selenite and ascorbic acid and further RΔF spheres were added as a capping agent to stabilize the NPs.

2.3.1. Characterization of RΔF-SeNPs. The prepared NPs were characterized by utilizing microscopic as well as spectroscopic methods as mentioned below.

2.3.1.1. UV-visible spectroscopic studies. A diode assortment spectrophotometer (Shimadzu UV-2600) was utilized for determining the UV/visible spectrum of the NPs and this was recorded using a 1 cm quartz cuvette in the wavelength range spanning from 220–800 nm.

2.3.1.2. Dynamic light-scattering (DLS) studies. The distribution of size and polydispersity index (PDI) of the NPs was assessed by utilizing DLS (Model ZEN5600, UK) at an angle of 173°. DLS readings were taken at RT.

2.3.1.3. Transmission electron microscopy (TEM). For TEM analysis, the NPs were dropcast onto copper grids and were analyzed at 120 kV, utilizing a JEOL JEM-2100 TEM. The micrographs were recorded digitally and processed utilizing the microscope camera.

2.3.1.4. Energy-dispersive X-ray (EDX) studies. EDX studies were performed using the EX-250 system (Horiba) to determine the elements present in the RΔF-SeNPs.

2.3.1.5. Fourier transform infrared spectroscopy (FT-IR). Fourier transform infrared spectroscopy (FT-IR) of synthesized samples was carried out using an Equinox 55 IR spectrometer in the wavelength ranging from 4000–400 cm^{-1}.

2.3.1.6. X-ray photoelectron spectroscopy (XPS). XPS measurement was carried out utilizing a Thermo Fisher scientific K-Alpha spectrometer. An electron gun with low energy was utilized for the stagnant charge compensation.

2.3.1.7. Determination of NP stability. The stability of NPs was assessed in DMEM/F12 medium consisting of 10% fetal bovine serum (FBS) for 7 days by employing DLS analysis.

2.3.2. Preparation of FF, Ac-PHF6 and Aβ42 peptide fibrils. FF fibrils were formed as described earlier.[34] Briefly, 4 mg FF was solubilized in 1,1,1,3,3,3-hexafluoro-2-propanol (HFIP) (50 μL) and then peptide assembly was initiated by adding distilled water (950 μL) to the HFIP solution of the peptide. The sample was kept stationary for 1 h and was allowed to aggregate. Ac-PHF6 fibrils were generated as described in the literature.[45] Fibrils were formed by incubating the peptide (3 mg mL^{-1}) for 72 h at 70 °C. Both the peptide-derived fibrils were characterized by following various assays and techniques, for instance a thioflavin T (ThT) assay, SEM, confocal microscopy, and circular dichroism (CD). Aβ42 peptide fibrils were formed as explained in the literature earlier.[46] Briefly, Aβ42 in powdered form was initially placed in 1 mg mL^{-1} HFIP. Furthermore, the prepared solution was maintained for 2 h at 4 °C in a properly sealed vial under shaking conditions for dissolution. Prior to use, the thin transparent, clear layer of Aβ42 acquired after HFIP evaporation was dissolved in PBS and the sample was sonicated for 60 seconds (s) in the water bath. Furthermore, for enabling the aggregation of Aβ42 fibrils, the prepared sample was incubated for 72 h, at 37 °C. The formed fibrils were characterized by using TEM, ThT, and confocal microscopy.

2.4. Studying the disaggregation propensity of RΔF-SeNPs towards the peptide fibrils

The disaggregation propensity of the RΔF-SeNPs towards peptide fibrils was investigated by utilizing various methods that include ThT assay, confocal microscopy, SEM, and CD spectroscopy.

2.4.1. Thioflavin T (ThT) assay. Fibrillation of FF, as well as Ac-PHF6, was assessed by a fluorescence-based ThT assay. This assay was utilized to determine the aggregation kinetics of the peptides as well as to decipher the disaggregation/inhibition propensity of the NPs towards the peptide aggregates. For the disaggregation assay, 20 mM ThT stock solution was prepared in phosphate buffered saline (PBS), and furthermore, the sample was syringe filtered (with a 0.2 μM filter) before being used. For experiments, 80 μL of pre-incubated peptide samples were withdrawn and incubated with 20 μL of 20 μM ThT. The plate was allowed to shaken for 60 s and the ThT spectrum was analyzed using a spectrofluorometer at an excitation wavelength of 420 nm and emission wavelength of 482 nm. FF (12 mM, 10 mM, 8 mM, 6 mM, 4 mM, and 2 mM) and Ac-PHF6 fibrils (100 μM, 75 μM, 50 μM, 25 μM, 5 μM, and 2.5 μM) at different concentrations were incubated individually with ThT (20 μM) to gain insight into their aggregation behavior. For the inhibition studies, NPs (SeNPs, RΔF NPs, and RΔF-SeNPs) were added to both the peptides (FF and Ac-PHF6) just after the initiation of their fibrillization process. This was analyzed by ThT assay.

2.4.2. Bis-ANS assay for determining the propensity of the NPs to disaggregate peptide-based amyloid fibrils. Bis-ANS is being used for the detection of amyloid fibrils in various studies.[47] To have a deeper idea about the amyloid disaggregation potential of the NPs, FF fibrils were incubated with SeNPs, RΔF NPs, and RΔF-SeNPs at RT for 24 h, on a rotary shaker at 30 rpm. Furthermore, 80 μL of pre-incubated samples were withdrawn and co-incubated with 20 μL of 50 μM Bis-ANS dye for 0.5 h. The plate was shaken for 60 seconds, and the UV-Vis spectra of the samples were taken in the wavelength range spanning from 350–650 nm using a spectrofluorometer.

2.4.3. Microscopic analysis

2.4.3.1. Electron microscopy. Microscopic studies were further carried out to assess the morphological and structural variations, if any, in the peptide fibrils incubated alone or with the NPs for a duration of 24 h. For the disassembly process, FF fibrils were incubated with different concentrations of NPs for 24 h at 37 °C on a rotary shaker maintained at 100 rpm. After the incubation period was over, aliquots of FF fibril-treated samples were analyzed by SEM by dropcasting them on silicon wafers. Ac-PHF6 fibrils treated with NPs were analyzed by using field emission scanning electron microscopy (FESEM) as mentioned below. FESEM was done to determine the morphological nature of the Ac-PHF6 fibrils alone or with RΔF-SeNPs. For the analysis, samples were dropcast on cleaned silicon wafers and further air-dried overnight. Before the examination, NPs were gold coated at 20 Pa for 90 s. Afterward, the prepared samples were observed and imaged under a field emission scanning electron microscope. Micrographs were further processed using JSM-IT300 software. The morphology of the aggregated Aβ42 peptide fibrils and furthermore the disassembly of the Aβ42 fibrils (20 μM) by RΔF-SeNPs were analyzed by TEM.

2.4.3.2. Confocal microscopy. ThT and Bis-ANS pre-stained samples of Ac-PHF6 and FF fibrils were incubated with NPs (RΔF-SeNPs, RΔF, SeNPs) at 100 rpm on the rotatory shaker for 24 h at 37 °C to determine the fibril disaggregation tendency of the NPs. The samples were next dropcast onto properly cleaned glass slides and were further imaged *via* confocal microscopy. Similarly, Aβ42 fibrils treated with NPs were imaged by confocal microscopy.

2.4.4. Circular dichroism (CD) analysis of the peptide fibrils carried out in the presence and absence of the NPs. Circular dichroism analysis was carried out to comprehend the secondary structure of the FF fibrils. The study was also carried out to determine the conformational perturbations taking place in the peptide fibrils in the presence of the NPs. For the study, FF fibrils were incubated with the NPs for 24 h and further CD spectra of the samples were determined after suitable sample dilution on a CD spectropolarimeter (in the wavelength range of 190–290 nm).

2.4.5. Chiral environment affects amyloid aggregation. The amyloid polypeptide shows enantiomer dependent behavior. Thus, herein we further used amino acids such as D-alanine (D-Ala) and L-alanine (L-Ala) to study their effect on the aggregation of Aβ. Next, we explored the ability of RΔF-SeNPs to inhibit amino acid enantiomer-induced Aβ42 aggregation. The enantiomer-induced Aβ42 aggregation was carried out as described previously.[48] Amyloid fibrils formed were placed onto a clean silicon wafer and were assessed by FESEM.

2.5. Cellular uptake of the NPs determined in SH-SY5Y cells

SH-SY5Y cells (10×10^4 cells per well) were first cultured in a sterile 6-well plate for a duration of 24 h. The cells were further treated with rhodamine-labeled RΔF NPs, SeNPs, and RΔF-SeNPs for 24 h, rinsed with PBS thrice, and fixed with paraformaldehyde (PFA) (4%) for 0.5 h. The cells were then stained with the nucleus-staining dye DAPI (1 μg mL^{-1}) for a duration of 5 minutes, rinsed with cold PBS thrice, and visualized through confocal microscopy.

2.6. Assessment of cytotoxicity of FF and Ac-PHF6 fibrils toward SH-SY5Y cells

Cytotoxicity of FF and Ac-PHF6 fibrils towards SH-SY5Y cells was assessed using an MTT assay. For the MTT assay, SH-SY5Y cells were cultured for 24 h in sterile 96-well microtiter plates as discussed above. Following this, cultured cells were incubated with FF fibrils (2 mM to 12 mM) in DMEM/F12 media devoid of serum for a period of 24 h at 37 °C. Fresh medium (200 μL) consisting of 5 mg mL^{-1} of MTT in PBS (20 μL) and cell culture medium (180 μL) was added to each well. Cells were then incubated for 4 h and their medium was discarded and supplanted with DMSO (100 μL) in every well to solubilize the formazan crystals. Afterward, the sample absorbance was recorded at 570 nm utilizing a microplate reader.

For the live/dead assay, cells were cultured for one day and afterward were incubated with varying concentrations of Ac-PHF6/FF fibrils. Cells were then washed with PBS thrice as well as incubated with live/dead cell culture assay reagents, calcein AM (2 μL mL^{-1}), and propidium iodide (PI) (2 μL mL^{-1}) for 0.5 h at 37 °C in the dark. The cells were further rinsed out with PBS to eliminate the unwanted color of the dye and were analyzed by confocal microscopy. Viable neuroblastoma cells stained with calcein AM and exhibited green fluorescence, whereas those stained with PI represented non-viable cells and exhibited red fluorescence.

2.7. Assessment of biocompatibility of RΔF-SeNPs towards SH-SY5Y and L929 cells

Cells were cultured as mentioned above. The cells were then co-incubated with varying concentrations of RΔF-SeNPs in serum-free DMEM/F12 media maintained at 37 °C for 24 h. The cell viability was next determined by MTT assay as mentioned above.

2.8. Determination of the protective effects exhibited by NPs towards fibril-generated toxicity in SH-SY5Y cells

SH-SY5Y cells (10 000 per well) were cultured as described above. After 24 h, cells were exposed to FF fibrils (12 mM in serum-devoid medium) alone or with RΔF NPs, SeNPs, and RΔF-SeNPs for a period of 24 h. After 24 h, a colorimetric-based MTT assay was executed to determine the cellular viability. Similarly, for Ac-PHF6 fibrils (100 μM), the cells were exposed to Ac-PHF6 fibrils alone or co-incubated with RΔF NPs, SeNPs, and RΔF-SeNPs for a period of 24 h. On a similar note, cells were incubated with Aβ42 fibrils with or without RΔF NPs, bare SeNPs, and RΔF-SeNPs. Next, they were washed with PBS thrice and incubated with fluorescence-based live/dead cell viability dyes, calcein AM, and PI for 0.5 h at 37 °C. The dye-stained cells were then washed with PBS to get rid of surplus dye and were analyzed by confocal microscopy. Similarly, resazurin assay was carried out to determine the protective effect of RΔF-SeNPs towards Aβ42 fibril-induced cytotoxicity in SH-SY5Y cells. In brief, 10 000 SH-SY5Y cells were seeded per well in a 96-well plate and the plate was incubated for 24 h. Cells were incubated with Aβ42 fibrils with or without RΔF-SeNPs for 24 h. After the incubation period, 20 μL of 2× resazurin stain was added to each well, and the plate was further incubated for 4 h. Fluorescence readings were taken with an excitation wavelength of 530 nm and an emission wavelength of 590 nm.

2.9. Estimation of the reduction of intracellular reactive oxygen species (ROS) produced by SH-SY5Y cells in the presence of Aβ42 fibrils

Free-radical/ROS generation in the presence of Aβ42 fibrils was accessed by dichlorodihydrofluorescein diacetate (DCFH-DA) assay. Briefly, cells were incubated with either Aβ42 fibrils only or with Aβ42 fibrils in the presence of bare RΔF NP, SeNPs, and RΔF-SeNPs in a serum-free medium for 24 h. Subsequent to incubation, cells were further treated with DCFH-DA (30 μM) for 0.75 h at 37 °C. These cells were further washed twice with PBS and were imaged *via* confocal microscopy.

2.10. Effect of NPs on peptide oligomers

The effect of NPs on peptide (FF and Ac-PHF6) oligomers was examined by using confocal microscopy. The formed oligomers were incubated with NPs at RT for 24 h on a rotatory shaker at 37 °C. These samples were also dropcast on glass slides and were further analyzed *via* confocal microscopy.

2.11. STZ-induced amyloid model generated in mouse N2a cells

For studying the role of STZ in triggering amyloidogenic properties in neural cells, mouse neuronal, N2a, cells were cultured using DMEM/F12 (1 : 1) medium with 12% FBS. Then 10 000 cells per well were cultured in a sterile 96-well plate for 24 h. Cells were then exposed to STZ for 48 h at different concentrations, *i.e.* 10 μM, 50 μM, 100 μM, and 1000 μM, as reported earlier.[37] Following treatment, the viability of the treated cells was evaluated *via* an MTT assay as stated above. For cell uptake studies, N2a cells (10×10^4 cells per well) were cultured as mentioned above. Cells were then incubated with rhodamine-labeled RΔF NPs, SeNPs, and RΔF-SeNPs for 24 h for studying their cellular uptake behavior. After the incubation duration was over, PBS was used to wash excess dye from the cells, and images were further taken utilizing ZEN blue software.

Similarly, for studying the effect of the NPs on STZ-induced amyloidogenic effects in N2a cells, the neural cells were incubated with STZ (1000 μM) only or accompanied either by RΔF-SeNPs, RΔF NPs, or SeNPs. The cell viability was then assessed using an MTT assay.

For the live/dead assay, N2a cells were cultured for 24 h and afterward were incubated with STZ (1000 μM) alone or along with RΔF-SeNPs, RΔF NPs, and SeNPs. The cells were further examined for live/dead assay following a similar procedure as mentioned above.

For the detection of amyloid aggregates inside STZ-treated N2a cells, an amyloid aggregate detection assay was carried out. Briefly, N2a cells were cultured on clean coverslips and were incubated with STZ (1000 μM) alone or with RΔF-SeNPs, RΔF NPs, and SeNPs for a duration of 48 h and after that fixed with PFA (4%) for 0.3 h at RT. Furthermore, cells were incubated with the solution (10 μM) for 0.3 h. Cells were finally rinsed with PBS thrice to eradicate any surplus stain and were then observed under a confocal microscope.

2.12. Determination of the BBB transport efficiency of RΔF-SeNPs

2.12.1. BBB transport efficiency of RΔF-SeNPs as determined *via* inductively coupled plasma-mass-spectrometry (ICP-MS). For the assay, the hippocampi of the mice were isolated, submerged in nitric acid, and heated at 80 °C for 24 h. Afterwards, the volume of the solution was adjusted to 6 mL employing nitric acid (2%), and the prepared samples were assessed by ICP-MS.

2.12.2. Biodistribution of NPs in mice. For determining the distribution of the NPs in mice, fluorescence imaging of the animals was carried out utilizing an *in vivo* fluorescence imaging system at an excitation of 789 nm and emission of 814 nm. For *in vivo* imaging, ICG (0.2 mL) labeled NPs (0.5 mg kg^{-1}) were intravenously administered to mice. The fluorescence images of entire mice were taken at 0, 24, 48, and 72 h after NP administration and isoflurane anesthetization (3% for induction and 1% for maintenance).

2.13. *In vivo* assessment of RΔF-SeNPs in the ICV-STZ-induced rat model

2.13.1. Animals. Adult male Sprague-Dawley (SD) rats were procured from our institutional animal facility. The animals were housed in a pathogen-free environment with a controlled temperature (23–25 °C), humidity (60 to 65%) and light–dark cycles (12 h), and *ad libitum* access to water and food. All the experimental protocols were approved by the Animal Ethics Committee of CSIR-Central Drug Research Institute, Lucknow, India, which follows the guidelines of Committee for the Purpose of Control and Supervision of Experiments on Animals (CPCSEA), in compliance with the International norms of the Indian National Science Academy (INSA). No humans were used in this study.

2.13.2. Stereotaxic injection of STZ. Pentobarbitone sodium (40 mg kg^{-1}, i.p.) was used to anesthetize the rats. Toe pinching was used to test the nociceptive reaction of the rats, prior to surgery. The rat's head was mounted on the stereotaxic frame by the ear canals and was fastened to the stereotaxic device (Stoelting Co., USA). To visualize the skull, a longitudinal incision was made on the head. The skull was thoroughly cleaned in order to locate the bregma. Using a drill, a small burr hole was made in the skull, and 5 μL of STZ (1 mg kg^{-1} dissolved in aCSF) was injected into the lateral ventricles (LVs) at stereotaxic coordinates of −0.8 mm anteroposterior (AP), ±1.5 mm mediolateral (ML), and −3.6 mm dorsoventrally (DV), measured from the bregma, *via* a Hamilton syringe with 28 gauze-sized needle, under a controlled flow rate (0.3 μL min^{-1}). To reduce backflow, the syringe was left in place after the injection, for an additional five minutes. A similar amount of artificial cerebrospinal fluid (aCSF) was administered into the lateral ventricles of the control group.

2.13.3. RΔF-SeNP administration into the animals. For the study, rats were arbitrarily classified into 4 groups with 6 animals in every group. A schematic methodology depicting the study design is illustrated in Scheme 2.

I group: Rats categorized in the control group were stereotaxically injected with CSF (5 μL), in each lateral ventricle.

II group: Rats stereotaxically injected with STZ (5 μL) in each ventricle (1 mg kg^{-1}) were categorized into the STZ-treated group.

III group: Rats were administered with RΔF-SeNPs (5 mg kg^{-1}, i.v.) in each ventricle on alternate days, beginning one week after STZ (5 μL) administration, and continuing for 21 days.

IV group: RΔF-SeNPs (i.v.) were administered at a dose of 5 mg kg^{-1} to rats for 21 days. The treatment commenced on a similar day as in group III.

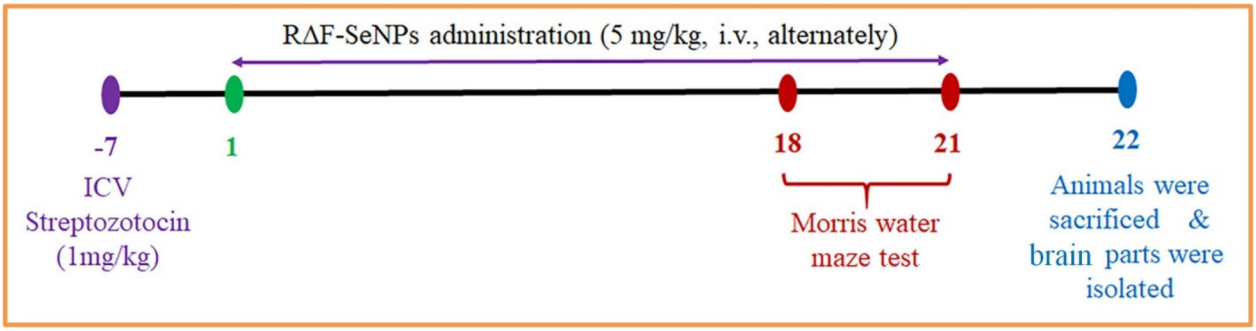

Scheme 2 Schematic illustration of the plan of *in vivo* experiments in the STZ-induced AD rat model.

2.13.4. Morris water maze test. Spatial learning and memory improvement in the rats after RΔF-SeNP administration was evaluated using the Morris water maze test as described previously.[49] The test was carried out in a spherical pool with 132 cm × 75 cm dimensions. A 15 cm diameter platform was concealed 1 cm beneath the water surface at a controlled temperature of 25 ± 0.5 °C in the pool. The sessions of the spatial, as well as learning, memory were conducted on days 18, 19, and 20 post RΔF-SeNP administration, followed by a probe test on day 21. The daily session comprised three 2 minute-long trials. On day 1 (session 1/1st learning stage), the rats were positioned in a water pool, and the trial was completed either when the rat had reached the display place or when the trial duration had lapsed. Similar trials were conducted in testing periods 2 and 3 for memory acquisition, and the latency to reach the display place was determined. The platform was removed, and the animals were evaluated for one minute on the fourth day of testing. ANY-maze software was used to record the escape latency time.

2.13.5. Immunohistochemical analysis. Prior to perfusion, a large dosage of sodium pentobarbital (50 mg kg^{-1}, i.p.) was given to the animals. Slow infusions of ice-cold PBS and 4% paraformaldehyde (PFA) were given transcardially to the rats. The brains were isolated from the skulls and stored overnight at 40 °C in PFA. Using 10%, 20%, and 30% sucrose, the brains were successively dehydrated throughout 72 h. Thick brain slices (30 μm) covering the prefrontal cortex as well as the hippocampus were cut utilizing a cryostat. The processing of free-floating parts was done as detailed in our earlier publication.[50] In summary, sections were washed thrice with Tris-buffered saline (TBS) followed by permeabilization with Tris-buffered saline with Tween (TBST) at RT, and then washed again with TBS. Any nonspecific binding of the target antibody to the tissue sections was blocked by pre-incubating the tissues with BSA (5%) in TBST at RT for 2 h. The sections were then treated with mouse anti-Aβ overnight at 4 °C. Sections were cleaned with TBS and further incubated with anti-mouse Alexa Fluor-488/494 secondary antibody for 2 h at RT in the dark. The sections were affixed onto clean, properly wiped glass slides and further incubated with DAPI mounting medium. Fluorescence intensity was measured using an inverted fluorescent microscope with a digital CCD camera and Image J software.

2.14. Hematoxylin and eosin (H&E) staining

It was carried out to assess the morphological alterations in the organs of the mice (*e.g.*, heart, liver, spleen, lungs, and kidneys) treated with SeNPs, RΔF NPs, and SeNPs. Organs treated with the NPs were collected from the mice 72 h post-injection and fixed in a formalin [10%] solution. These tissue sections were dewaxed with xylene and hydrated with ethanol. The tissues were left at room temperature for 1 h. Finally, all the tissue samples were embedded in paraffin blocks, sectioned into 5 μm slices, and stained with H&E dye for histological examination under a light microscope.

2.15. Statistical analysis

Data were obtained through three individual experiments and were analyzed statistically *via* a Kruskal–Wallis test followed by Dunn's multiple comparison tests. Significance levels are expressed as * $p < 0.05$; ** $p < 0.01$; *** $p < 0.001$. Data were displayed as mean ± SEM and assessed using GraphPad Prism. All results were quantified using one/two-way analysis of variance (ANOVA) followed by the Bonferroni *post hoc* test, and $P < 0.05$ was deemed statistically significant.

3. Results and discussion

3.1. Synthesis and characterization of RΔF-SeNPs

In the current work, we have used the dipeptide, RΔF-derived spheres as capping and stabilizing entities for the synthesis of the SeNPs. The synthesized dipeptide, RΔF, was analyzed by HPLC and mass spectrometry (Fig. S1A and S1B†). SeNPs were first synthesized *via* achieving a redox reaction between sodium selenite and ascorbic acid.[51] This process of SeNP formation resulted in the aggregation and precipitation of Se atoms. Therefore in order to stabilize the particles and prevent further aggregation, RΔF spheres were used as capping entities to generate stable SeNPs. The sample demonstrated an absorption maximum at 265 nm in UV-Vis spectroscopy (Fig. 1A) and this confirmed the formation of SeNPs.[52] The synthesized NPs were characterized for their stability and hydrodynamic size distribution. RΔF-SeNPs exhibited a hydrodynamic diameter of around 101 ± 30 nm with an average PDI of 0.180. However, the particle size of bare SeNPs was found to be 564 ± 30 nm

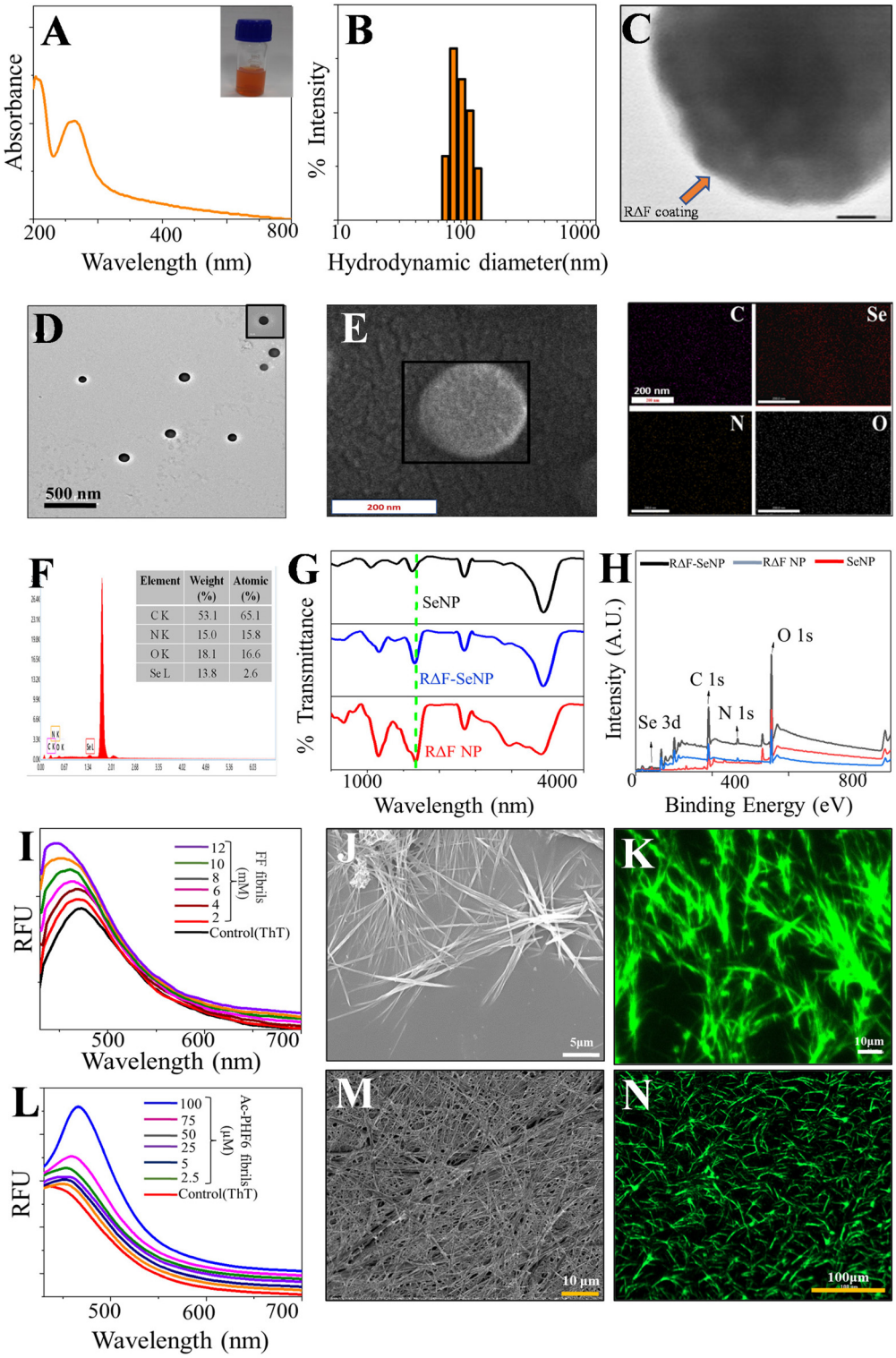

Fig. 1 Characterization of RΔF-SeNPs. (A) UV-vis spectrum of RΔF-SeNPs. (B) Dynamic light-scattering (DLS) profile of RΔF-SeNPs. (C) Electron microscopic image of NPs showing the RΔF coating. (D) Transmission electron microscopic image of RΔF-SeNPs. (E) EDS elemental mapping of RΔF-SeNPs (scale bar is 200 nm). (F) Elemental composition analysis of RΔF-SeNPs. (G) FTIR spectra of RΔF-SeNPs, RΔF NPs and SeNPs. (H) XPS spectra of SeNPs, RΔF NPs, and RΔF-SeNPs. Estimation of the aggregating propensity and fibril-forming capability of FF and Ac-PHF6. (I) Concentration-reliant fluorescence-based ThT assay of the fibrils. (J) SEM image of FF fibrils. (K) Confocal microscopic image of ThT pre-stained FF fibrils. (L) Concentration-dependent fluorescence-based ThT assay of Ac-PHF6. (M) FESEM image of Ac-PHF6. (N) Confocal image of Ac-PHF6 fibrils stained with ThT dye.

with an average PDI of 1. Thus, we found that the RΔF spheres could regulate the overall size and polydispersity of the SeNPs and it was observed that the size of the RΔF-SeNPs was significantly less as compared with the uncapped SeNPs (Fig. 1B). The RΔF coating also aided in the formation of more homogeneous structures with less PDI. In sync with our results, previous reports have suggested that the interaction of NH_3^+ functional groups of peptides/amino acids with negatively-charged SeNPs *via* electrostatic interactions may possibly be the driving factor for the fabrication of monodisperse and stable NPs.[51] Furthermore, the shape of the particles was examined by TEM analysis. Bare SeNPs exhibited irregular shapes and were found to be in clusters as shown in Fig. S3A,† whereas RΔF NPs were found to have uniform vesicular structures as shown in Fig. S3B.† RΔF-SeNPs demonstrated the presence of spherical structures with a surrounding halo (Fig. 1C and D). Furthermore, the presence of Se and N in the RΔF-SeNPs was confirmed by SEM-EDS mapping analysis (Fig. 1E). Elemental composition analysis of the particles was carried out utilizing energy-dispersive X-ray spectroscopy (EDX). Data revealed the presence of Se (13.8%), N (15%), C (53.1%), and O (18.1%) in the structures. The presence of N atoms further confirmed peptide vesicle capping on the SeNPs (Fig. 1F). Next, FTIR spectroscopy was performed to assess the surface functional groups of the NPs. The IR spectrum of the RΔF NPs showed a characteristic amide carbonyl peak at 1662 cm^{-1}.[53] RΔF-SeNPs also exhibited the presence of the amide carbonyl peak at 1662 cm^{-1}. Thus, our IR analysis results confirmed the existence of the dipeptide-coating on the surface of the SeNPs (Fig. 1G). XPS spectra also showed the existence of a N 1s peak at 402 eV in the spectrum and affirmed the conjugation of RΔF NPs onto the surface of the SeNPs (Fig. 1H). RΔF-SeNPs were found to be stable in biological media containing 10% FBS for up to 7 days, depicting their high stability (Fig. S4†).

3.2. Synthesis of FF and Ac-PHF6

FF was analyzed using HPLC and mass spectrometric analysis as mentioned in ESI S3.† AcPHF6 (Ac-VQIVYK-NH_2) was analyzed by mass spectrometry (Fig. S5†).

3.3. Determination of the aggregating potential of FF and Ac-PHF6

Thioflavin T (ThT) dye depicts fluorescence augmentation upon adherence to amyloid fibrils.[54] The aggregation and fibril-forming potential of FF and Ac-PHF6 were examined *via* a ThT assay. For the ThT assay, different concentrations of FF and Ac-PHF6 were incubated individually with ThT (20 μM) to explore their aggregating behavior. Like other amyloidogenic peptide/protein-based studies, the aggregated peptides demonstrated an increase in their fluorescence intensities in the presence of the dye. It was seen that the peptide fibrils showed a concentration-reliant enrichment in their ThT fluorescence intensities with the exhibition of maximum fluorescence intensity at 12 mM and 100 μM for FF and Ac-PHF6 respectively. This confirmed that both FF and Ac-PHF6 could form amyloid-type aggregates (Fig. 1I and L), along with exhibiting a concentration-dependent aggregating behavior. Furthermore, we also analyzed the fibril-forming potential of the peptides *via* microscopic analysis. Microscopic images revealed the generation of fibrillar aggregates by the peptides (Fig. 1J and M) as evidenced *via* FESEM and TEM analysis. Fluorescence imaging also depicted the presence of bundles of amyloid fibrils in the case of both peptides (Fig. 1K and N).

3.4. Determination of the disaggregating potential of NPs towards FF fibrils

We next utilized a fluorescence-based ThT assay to determine the anti-aggregating behavior of SeNPs, RΔF NPs, and RΔF-SeNPs towards FF fibrils. As depicted in Fig. 2A, FF fibrils alone exhibited a high fluorescence intensity, whereas those incubated with SeNPs and RΔF NPs demonstrated a decline in their fluorescence intensities. The maximum decline in the fluorescence intensity was achieved in the case of FF fibrils incubated with RΔF-SeNPs for a period of 24 h. Furthermore, RΔF-SeNPs abrogated FF aggregation in a concentration-dependent way. The higher the concentration of RΔF-SeNPs, the greater their disaggregating propensities towards FF fibrils (Fig. 2B). We further assessed the disaggregating potential of the NPs towards FF fibrils *via* a Bis-ANS assay. Various studies report on the utility of Bis-ANS for the analysis of amyloid-like fibrils.[47] In the assay, FF fibrils were incubated with SeNPs, RΔF NPs, and RΔF-SeNPs for 24 h. Our results revealed that the dipeptide fibrils demonstrated a maximum decline in their fluorescence intensity when treated with RΔF-SeNPs (Fig. S6A†). Notably, a disaggregation of FF fibrils by RΔF-SeNPs was achieved at 50 μg mL^{-1} (Fig. S6B†) of RΔF-SeNPs. We further determined the secondary structure of FF fibrils in the presence of the NPs. FF fibrils exhibited a CD peak at 193 nm corresponding to $\pi \rightarrow \pi^*$ transition, and a broad positive band centered at 219 nm indicating $n \rightarrow \pi^*$ transition.[55] However, after 24 h of incubation of FF fibrils with SeNPs and RΔF NPs, a slight conformational variation in the secondary structure of FF fibrils was observed. This was evidenced by a slight shift in the bands and their intensities when the fibrils were being incubated with SeNPs and RΔF NPs. Interestingly, after the addition of RΔF-SeNPs, FF fibrils exhibited a remarkable distortion in their secondary structure (Fig. 2C).

Furthermore, we continued to determine the effect of the NPs on the agglomeration of FF fibrils by utilizing SEM analysis. Compared with the untreated FF fibrils, NP-treated fibrils demonstrated a loss in their fibrillar structures. Incubation of the peptide fibrils with RΔF-SeNPs led to a pronounced loss of their fibrillar structures. Only spherical, small, and amorphous structures were observed in this case. Our results elicited that the fibril-dislodging potential of RΔF-SeNPs towards FF fibrils was higher than those of SeNPS and RΔF NPs (Fig. 2D). Moreover, RΔF-SeNPs could modify FF fibrils into smaller, amorphous structures, as apparent in the images. Thus, these results depicted that RΔF-SeNPs could disaggregate FF fibrils by trapping them in the form of amorphous and non-specific structures (Fig. 2E).

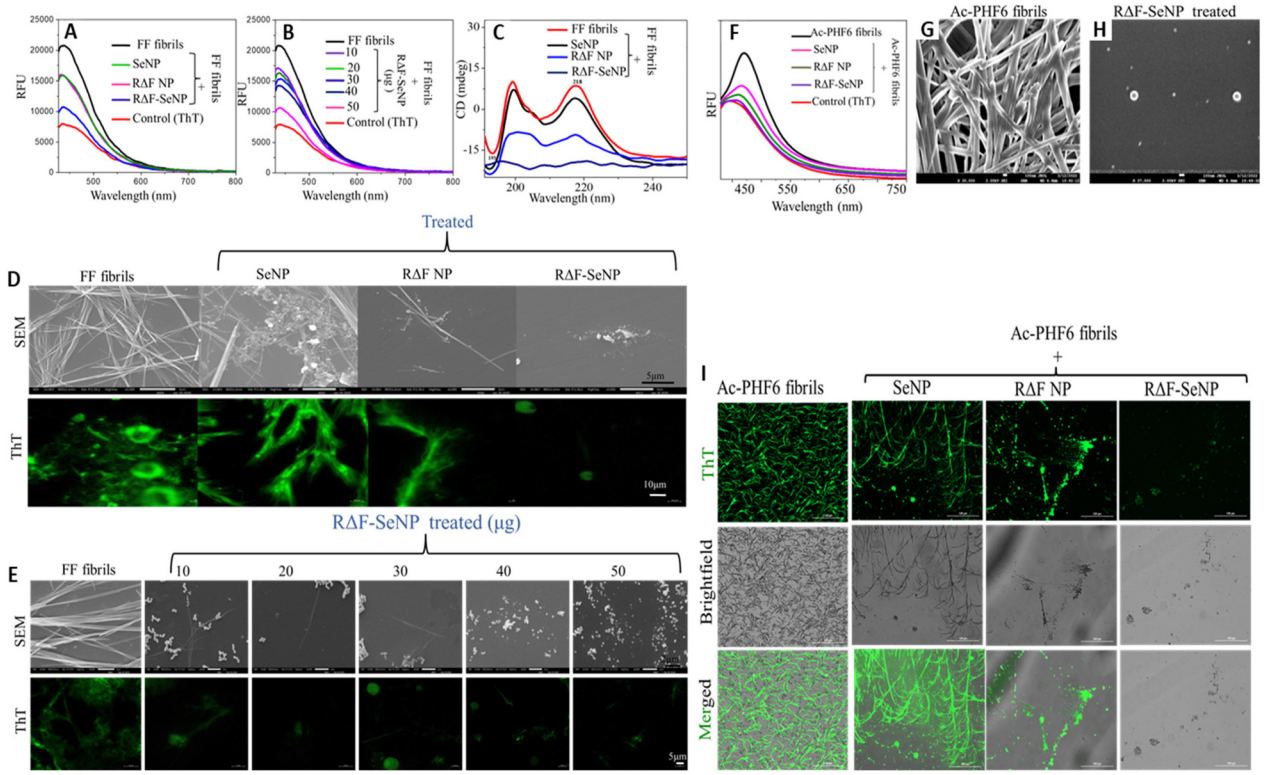

Fig. 2 (A) ThT spectra of FF fibrils co-incubated with SeNPs, RΔF NPs, and RΔF-SeNPs. (B) ThT spectra of FF fibrils treated with different concentrations of RΔF-SeNPs. (C) CD spectra of FF fibrils and FF fibrils incubated with SeNPs, RΔF NPs, and RΔF-SeNPs. (D) SEM and confocal-microscopic images of ThT-stained FF fibrils incubated with SeNPs, RΔF NPs, and RΔF-SeNPs. These results pointed toward the potential disaggregation of FF fibrils by RΔF-SeNPs. (E) Concentration-dependent disaggregation of FF aggregates when co-incubated with RΔF-SeNPs. Disassembly of Ac-PHF6 fibrils in the presence of the NPs. (F) ThT assay showing aggregation curves of Ac-PHF6 fibrils incubated for 24 h either alone or with SeNPs or RΔF NPs or RΔF-SeNPs. (G) FESEM of Ac-PHF6 fibrils incubated alone and (H) Ac-PHF6 fibrils incubated with RΔF-SeNPs. (I) ThT fluorescence images of Ac-PHF6 fibrils taken after an incubation period of 24 h either alone or with NPs. A complete attenuation of Ac-PHF6 fibrils was observed in the presence of RΔF-SeNPs.

Furthermore, we assessed the disaggregating effect of the NPs on ThT-stained FF fibrils by utilizing microscopic analysis. FF fibrils incubated for 24 h without any assembly modulators retained their aggregated structures. FF fibrils co-incubated with SeNPs and RΔF NPs also illustrated the presence of aggregated structures like those observed in the case of neat FF, but to a lesser extent. However, FF fibrils incubated with RΔF-SeNPs (50 μg mL^{-1}) demonstrated a complete loss of the fibrillar aggregates. Fibrils incubated with RΔF-SeNPs further depicted a concentration-dependent disintegration of the aggregates (Fig. 2E). As we moved ahead from lower to higher concentrations (10 μg to 50 μg) of RΔF-SeNPs, we observed the formation of short fibrils, a combination of short fibrils and spherical particles, and finally the generation of smaller, spherical particles. This presented the possibility that the NPs decreased FF aggregation and further constrained the peptide into spherical structures. To substantiate the findings of the SEM and ThT-based microscopy, we used a Bis-ANS assay to monitor fibril formation with or without NPs, as shown in Fig. S6C and S6D.†

As hypothesized, FF alone showed the generation of distinct fibrillar aggregates, and incubation of the preformed peptide fibrils with RΔF-SeNPs demonstrated a concentration-dependent decline in the fibrillar structures. These results correlated with our SEM and ThT-based microscopic analysis. Such disruption of FF fibrils could be hypothesized to have occurred due to the formation of hydrophobic, aromatic, and hydrogen-bonding interlinkages between the aromatic ring containing the amphipathic molecule (RΔF) and the peptide aggregates.[51] Nanoparticles have been widely used to reduce the severity of amyloid aggregation.[56] Nanoparticles with specific surface chemistry are capable of retarding the fibrillation process.[57] It was reported in previous studies that peptides consisting of aromatic moieties could intercalate between the target amyloid aggregates, and partially swap the original amino acids in mediating the π–π stacking interactions, and thus have been shown to interfere with amyloid aggregation.[58] In a similar manner, aromatic residues of peptides and other small molecules (polyphenols) have been shown to interfere with the self-assembly and aggregation propensity of amyloidogenic peptides. For instance, polyphenols bearing aromatic residues such as epigallocatechin gallate (EGCG) inhibited the fibrillogenesis of pancreatic amyloid fibrils in human islet amyloid polypeptide (hIAPP), α-synuclein (α-syn) and Aβ42 *via* directly

binding to the natively unfolded polypeptides and thus preventing their conversion into toxic, on-pathway aggregation intermediates.[59–61] In a similar way, the naphthoquinone–tryptophan hybrid was shown to inhibit the fibrillogenesis of various amyloidogenic peptides such as Aβ42, IAPP, tau, and α-syn both under *in vitro* and *in vivo* conditions.[61,62] A tryptophan–galactosylamine hybrid inhibited as well as disaggregated the amyloid fibrils of Aβ42 and hIAPP peptides and thus reduced the toxicity associated with these aggregates.[63] Arginine has been shown to serve as a potential inhibitor of protein aggregates (Aβ42 and tau), and furthermore, polypeptides equipped with arginine moieties have been shown to elicit inhibitory effects on the formation and cytotoxicity of various protein aggregates.[64] Several arginine-rich peptides, such as RRRA, RRRL, and RFRK, were found to inhibit amyloid oligomerization. The inhibitory potential of RFRK was considered to be due to the presence of the phenylalanine residue. The phenylalanine residue became bound to the phenylalanine residue of Aβ *via* cation–pi interactions, thereby intensifying the interaction between the inhibitor and the Aβ.[65] Hybrid molecules (7-amino-4 trifluoromethyl coumarin and thiobenzyl ester) combined with peptide-bearing arginine residues resulted in destabilization of the Aβ fibrils and were found to bind to Aβ fibrils *via* hydrogen bonding through their guanidinium moieties.[66]

Additionally, several earlier studies have reported that the interactions between the NPs and the amyloid fibrils are strengthened in the presence of Se atoms and thus an overall synergistic mode of heightened anti-aggregating activity can be envisaged between the RΔF-SeNPs and the peptide aggregates.[67]

3.5. Determination of the disaggregating potential of NPs towards Ac-PHF6 fibrils

Another major hallmark of AD is the aberrant hyperphosphorylation of the tau protein, which has been demonstrated to promote protein aggregation. This further leads to the detachment of tau from the microtubules, which consequently causes the disassembly of the same due to its reduced microtubule-binding capacity.[68,69] The protein assembles into fibrillar aggregates, thus forming insoluble noxious amyloid deposits known as paired helical filaments (PHFs) and neurofibrillary tangles (NFTs).[70] The accumulation of NFTs has been found to be associated with neurodegenerative pathologies and is implicated in the brisk promulgation of the disease.[71] The commencement of tau protein aggregation is considered to be majorly mediated by the hexapeptide ^{306}VQIVYK^{311} (PHF6), situated in the third repeat of the microtubule-binding portion of the tau protein.[37,38] Cryo-EM structures of tau filaments depicted the N-terminal region of the cross-β-structure of the protein to be produced by the PHF6 fragment and it has been exemplified that the hexapeptide is necessary for manifesting the self-assembly of the tau protein.[72] This hexapeptide is considered as a model to mimic the full-length protein tau, because of its ability towards initiating tau aggregation and thus forming toxic fibrils, synonymous to those of tau filaments in the brains of AD patients.[73,74] Therefore, the hexapeptide mimics the whole tau protein that has widely been used as a target for developing/identifying potent modulators of tau fibrillization.[75]

Certain molecules can be used for the disaggregation of mature fibrils which are already prevailing in the brains of AD patients. So, we also compared the capability of SeNPs, RΔF NPs, and RΔF-SeNPs to disrupt Ac-PHF6 fibrils. The preformed Ac-PHF6 fibrils were incubated with NPs for 24 h. A ThT fluorescence assay was next carried out to monitor the fibril dislodging kinetics of the NPs. Fibrils incubated with RΔF-SeNPs demonstrated maximum disassembly as compared with bare SeNPs and RΔF NPs (Fig. 2F). Aggregation of the Ac-PHF6 peptide was further assessed by FESEM. Ac-PHF6 alone demonstrated the formation of dense fibrillar mesh-like networks (Fig. 2G). Disaggregation studies were conducted to comprehend the effect of RΔF-SeNPs on the Ac-PHF6 peptide fibrils. Disaggregated fibrils were further analysed using FESEM. The peptide fibrils co-incubated with RΔF-SeNPs showed a complete loss of their fibrillar structures (Fig. 2H).

Similarly, to further demonstrate the fibril dislodging potency of our NPs, a confocal microscopic analysis was carried out. Our results revealed that, in the presence of RΔF NPs, the peptide fibrils showed minor disassembly, and some amounts of small broken fibrils were observed. However, complete fibril disassembly was observed when Ac-PHF6 fibrils were co-incubated with RΔF-SeNPs (Fig. 2I). This revealed that RΔF-SeNPs could efficiently disassemble pre-formed Ac-PHF6 fibrils.

3.6. Determination of the inhibitory potential of NPs towards the amyloid-based model (FF and Ac-PHF6)

A potent anti-amyloidogenic molecule should inhibit the formation of amyloid aggregates and disintegrate the pre-formed fibrils.[76–78] Therefore, we also explored the inhibition potency of RΔF-SeNPs against peptide-based amyloid models (FF and Ac-PHF6) using the ThT fluorescence assay. As depicted in Fig. S7A,† FF fibrils alone exhibited high ThT fluorescence intensity, thus eliciting the formation of fibrillar aggregates. FF fibrils co-incubated with SeNPs and RΔF NPs demonstrated a decrease in their fluorescence intensities. However, the maximum decline in the fluorescence intensity was achieved in the case of FF fibrils incubated with RΔF-SeNPs, thus depicting an inhibition of the FF aggregation/fibrillation process. Similarly, Ac-PHF6 fibrils also showed the formation of fibrillar aggregates. RΔF NPs and SeNPs exhibited inhibition of the fibrillization process of Ac-PHF6 fibrils but it was at a lesser degree as compared with the RΔF-SeNPs (Fig. S7B†). Thus, our results demonstrated that RΔF-SeNPs could negatively interfere with the peptide fibrillation and aggregation process.

3.7. Determination of RΔF-SeNPs for inhibiting amino acid enantiomer-induced Aβ42 aggregation

It was found that RΔF-SeNPs could inhibit the enantiomer-induced aggregation of Aβ42 fibrils. RΔF-SeNPs inhibited

D-alanine-induced aggregation (Fig. S8C†), where the amyloid fibrils were completely disaggregated as compared with the D-alanine-induced aggregation in the absence of RΔF-SeNPs (Fig. S8B†). However, we observed that L-Ala did not affect the amyloid aggregation process (Fig. S8D†) and in the presence of RΔF-SeNPs, the fibrils remained disaggregated (Fig. S8E†).

3.8. Determination of cellular uptake of the NPs in SH-SY5Y cells

To be utilized as a prospective therapeutic moiety, it is essential that NPs should gain successful entry inside the neural cells. Thus, we next explored the possibility of RΔF-SeNPs for getting internalized into neuroblastoma, SH-SY5Y cells. To attain this, SH-SY5Y cells were treated with rhodamine 6G-labeled RΔF-SeNPs, RΔF and SeNPs for a duration of 24 h. This was followed by imaging the samples under a confocal microscope. Images revealed the presence of bright intra-cellular fluorescence in the case of cells treated with RΔF-SeNPs. Moreover, intracellular fluorescence was also observed in the case of cells incubated with RΔF NPs, thus suggesting the capacity of these NPs to gain entry inside the cells. However, cells treated with only SeNPs did not exhibit any significant intra-cellular fluorescence, depicting their poor cellular uptake behavior. Further quantification of the intracellular fluorescence intensity using confocal microscopy depicted maximum cellular uptake in the case of the RΔF-SeNPs, followed by RΔF spheres. It could be hypothesized here that RΔF-SeNPs demonstrated higher cellular uptake due to their smaller size as compared to bare RΔF NPs. Thus, it could be inferred here that RΔF-SeNPs exhibited successful cellular uptake and accumulation inside neural cells and carry the potential to be used as possible neurotherapeutic entities (Fig. 3A and B).

3.9. Assessment of cytotoxicity of peptide fibrils toward SH-SY5Y cells

Accretion as well as aggregation of Aβ peptides causes neuronal death, finally leading to cognitive dysfunction in AD.[79] Thus, we also tried to determine the cytotoxicity of Ac-PHF6 and FF fibrils toward SH-SY5Y cells at various doses. As shown in Fig. 3C and E, a dose-dependent decline in cell viability was seen for both the amyloid fibrils. Concerning the untreated control, a 50% reduction in the viable cells was found in the case of cells treated with 100 μM of Ac-PHF6 fibrils and 12 mM of FF fibrils. This was in agreement with our previous reports, where we have shown the toxic nature of FF fibrils toward SH-SY5Y cells.[34]

3.10. Determination of the biocompatibility and protective effects of NPs towards fibril-associated toxicity in SH-SY5Y cells

Before determining the neuroprotective effects of NPs toward peptide-fibril-induced toxicity, we first studied whether RΔF-SeNPs were compatible with SH-SY5Y cells through an MTT assay. As shown in Fig. S9A,† it was observed that the cellular viability in the case of RΔF-SeNP-treated cells was as high as 80% as compared with the untreated control cells, confirming their non-cytotoxic nature towards the neuronal cells. We also evaluated whether these hybrid RΔF-SeNPs were biocompatible toward fibroblast, L929 cells, *via* a colorimetric MTT assay. As depicted in Fig. S9B,† cells treated with RΔF-SeNPs were found to be approximately 92% viable as compared with untreated control cells. Thus, it was confirmed that RΔF-SeNPs were non-cytotoxic toward normal fibroblast cells. Moreover, RΔF-SeNPs were found to be compatible with SH-SY5Y cells as evident through resazurin assay. The resazurin assay (Alamar Blue assay) is a simple, rapid, and sensitive measurement for determining the viability of cells. Viable cells are metabolically active and are able to reduce, *via* mitochondrial reductase, the nonfluorescent dye resazurin to the strongly-fluorescent dye resorufin. The fluorescence is directly proportional to the number of viable cells.[80] As shown in Fig. S9C,† it was observed that the cellular viability in the case of RΔF-SeNP-treated cells was as high as 85% as compared with the untreated control cells, confirming their non-cytotoxic nature towards the neuronal cells.

We next continued to assess if RΔF-SeNPs could protect SH-SY5Y cells from FF fibril-induced cell toxicity. SH-SY5Y cells were treated with FF fibrils (12 mM) and RΔF-SeNPs simultaneously at 37 °C for 24 h and their endurance rate was analyzed by MTT assay. The outcome showed that treatment of SH-SY5Y cells with FF fibrils and RΔF-SeNPs simultaneously displayed an extensive decrease in FF-generated cytotoxic effects. In this condition, cell viability was again restored to around 90% after the co-treatment duration of 24 h, signifying that RΔF-SeNPs were able to shield the neural cells from toxic FF fibrils as shown in Fig. 4A. Increasing doses of RΔF-SeNPs resulted in a dose-reliant inhibition of FF fibril-originated toxicity in the SH-SY5Y cells as shown in Fig. S10A.† Furthermore, SH-SY5Y cells that formerly exhibited a deformation in their cellular structure in the proximity of FF fibrils demonstrated a re-establishment of their well-organized shape following treatment with RΔF-SeNPs in a concentration-reliant way (Fig. S10B†). Furthermore, it could be probably hypothesized that, enriched with the potential to rescue neuroblastoma cells from fibril (FF) generated toxicity, RΔF-SeNPs could serve as prospective anti-amyloid moieties. Our results further revealed that, in comparison with RΔF-SeNPs, SeNPs and RΔF NPs were comparatively less effective in rescuing neural cells from FF fiber-associated cytotoxicity. Moreover, these data were further supported by microscopic analysis, as shown in Fig. S11.†

Moreover, to supplement the data obtained from the MTT assay, a fluorescence-dependent live/dead cell viability evaluation of cells was carried out. Our data revealed that FF fibrils alone (12 mM) demonstrated a noteworthy quantity of red-fluorescent cells, signifying their cytotoxic nature. SH-SY5Y cells co-incubated with peptide fibrils (FF) and bare SeNPs also exhibited some red fluorescence along with the presence of viable green-fluorescing cells. RΔF NP-treated cells exhibited less red fluorescence, whereas RΔF-SeNP-treated cells expressed negligible red fluorescence with a copious amount of green-fluorescing cells. Thus, the higher green fluorescence

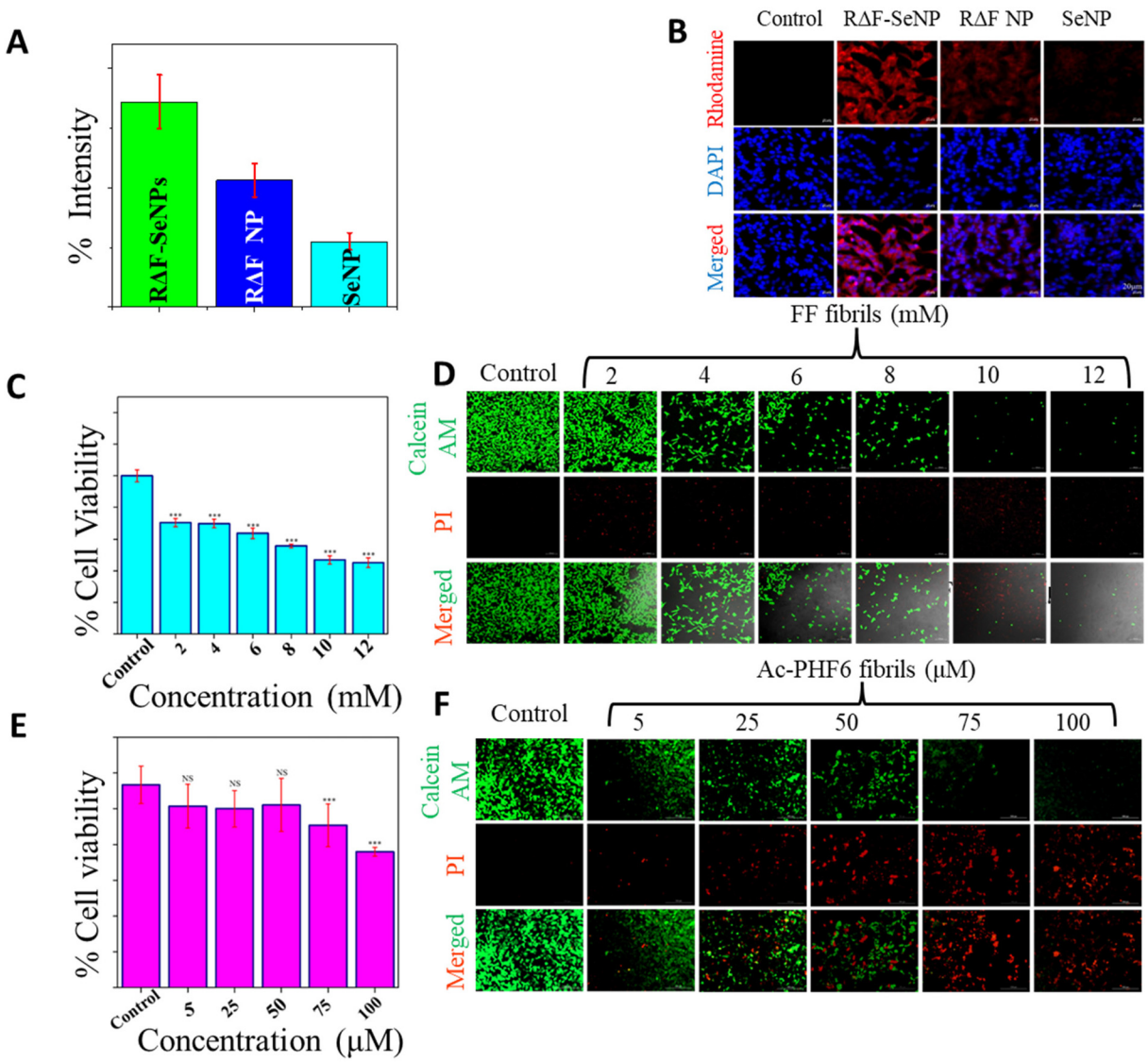

Fig. 3 (A) Determination of NP uptake in SH-SY5Y cells. (B) Confocal microscopic images showing the uptake of rhodamine 6G-labeled SeNPs, RΔF NPs, and RΔF-SeNPs in SH-SY5Y cells after a treatment period of 24 h. Scale bar = 20 μm. (C) Effect of FF fibrils on the viability of neuroblastoma, SH-SY5Y, cells after 24 h exposure as determined using an MTT assay. (D) Effect of FF fibrils on neural cell viability as assessed *via* a fluorescence-based calcein AM/PI assay (scale bar = 100 μm). (E) Effect of Ac-PHF6 fibrils on the viability of cells after 24 h, as examined by a fluorescence-based calcein AM assay. (F) Live/dead assay to detect the toxicity of different concentrations of Ac-PHF6 fibrils towards SH-SY5Y cells. For both the peptide fibrils, enrichment of the peptide concentration in the culture media resulted in a decline in the cellular viability, suggesting a concentration-dependent toxic effect of fibrils on SH-SY5Y cells (scale bar 200 μm). The data are represented as mean ± SD. Statistical analysis was carried out using a Kruskal–Wallis test followed by a Dunn's multiple comparison test. Significance levels are expressed as * $p < 0.05$; ** $p < 0.01$; *** $p < 0.001$.

exerted by the RΔF-SeNPs confirmed their neuroprotective effects (Fig. 4B). Collectively, this result was in accord with the outcomes obtained from our fibril disaggregation (*in vitro*) assays portraying an increased potency of RΔF-SeNPs to dislodge both the amyloid fibrils.

We further continued to assess the protective effect exerted by the NPs against Ac-PHF6 (100 μM) fibril-induced cytotoxicity in SH-SY5Y cells. For this, cells were incubated with Ac-PHF6 fibrils with or without NPs for 24 h at 37 °C, followed by evaluating the cellular survival by carrying out a fluorescence (calcein AM/PI) assay. It was observed that, on incubating the cells with Ac-PHF6 fibrils (100 μM) alone, a 50% reduction in their cellular viability relative to the control cells was observed. In contrast, the co-incubation of SH-SY5Y cells with Ac-PHF6 fibrils (100 μM) and RΔF-SeNPs showed a considerable decrease in their cytotoxic effects, with cell viability being restored to nearly 90% in the presence of RΔF-SeNPs. This verified that RΔF-SeNPs were able to safeguard the SH-SY5Y cells from the toxic aggregates (Fig. 4C). Comparatively, SeNPs and RΔF NPs were less effective in rescuing cells from Ac-PHF6 fibril-induced cytotoxicity, as demonstrated in Fig. 4D.

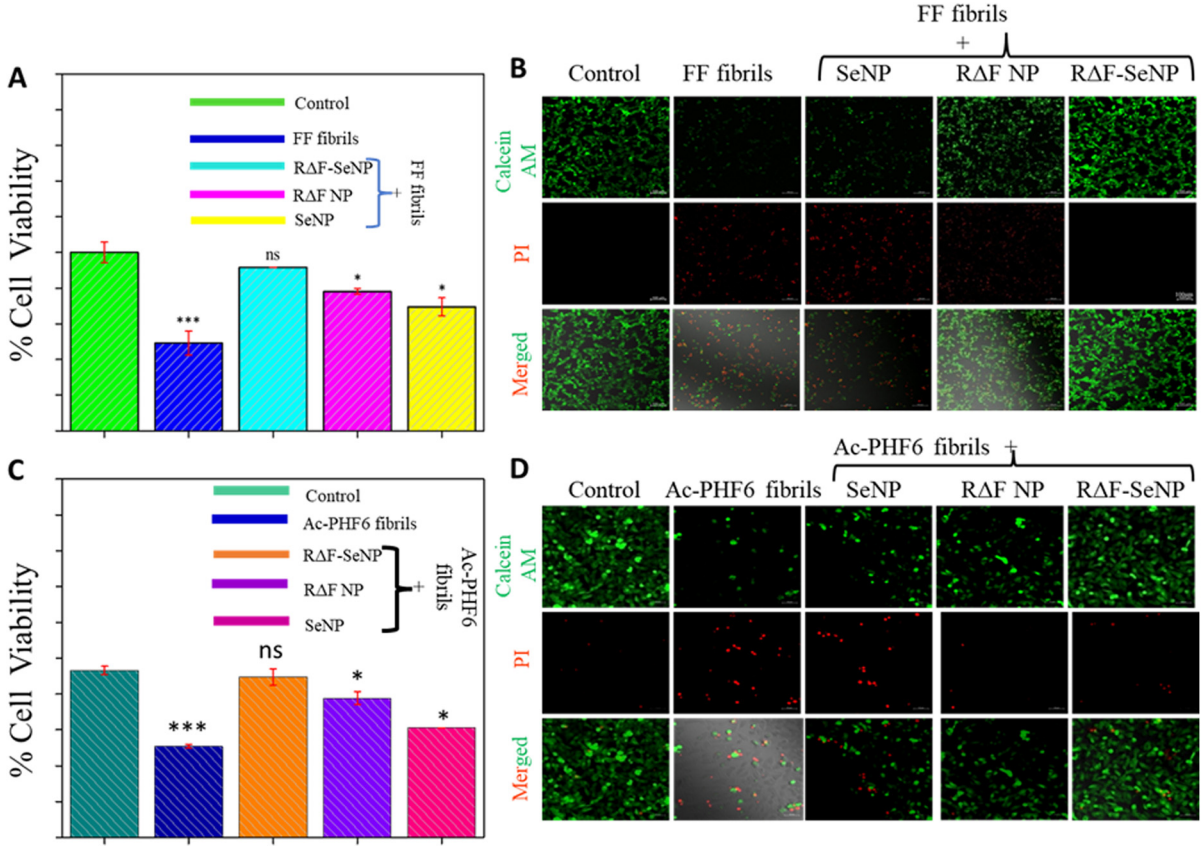

Fig. 4 (A) Protective role played by SeNPs, RΔF NPs, and RΔF-SeNPs against FF fibril-induced cytotoxicity in SH-SY5Y cells. (B) Confocal fluorescence microscopic images of calcein AM/PI-stained cells following co-treatment for 24 h with FF fibrils along with SeNPs, RΔF NPs, and RΔF-SeNPs (scale bar ~100 μm). The data are represented as mean ± SD. Statistical analysis was carried out using a Kruskal–Wallis test followed by a Dunn's multiple comparison test. Significance levels are expressed as * $p < 0.05$; ** $p < 0.01$; *** $p < 0.001$. (C) The protective role played by SeNPs, RΔF NPs, and RΔF-SeNPs against Ac-PHF6 fibril-produced cytotoxicity in SH-SY5Y cells. (D) Live/dead cell viability images of cells obtained following treatment with SeNPs, RΔF NPs, and RΔF-SeNPs in the presence of Ac-PHF6 fibrils (scale bar ~50 μm). The green color of the cells corresponds to live cells and the red color of the cells depicts dead cells.

3.11. Determination of the disaggregating potency of NPs towards Aβ42 fibrils

After determining the anti-amyloidogenic properties of RΔF-SeNPs towards FF fibrils and Ac-PHF6 fibrils, we next tried to explore and validate the disaggregating tendency of RΔF-SeNPs towards Aβ42 aggregates. With this goal, we initially explored the aggregation propensity of Aβ42 peptide *in vitro*, using ThT, TEM and confocal microscopy. Our results illustrated the formation of dense fibrillar assemblies by Aβ42 as shown in Fig. 5A and 5B. TEM analysis was also used to decipher the anti-aggregating tendency of our NPs. The disaggregation study results depicted that Aβ42 fibrils co-incubated with RΔF-SeNPs showed a complete disaggregation of the fibrillar assemblies (Fig. 5B). Next, we assessed the propensity of the NPs to disrupt Aβ42 fibrils by co-incubating them with Aβ42 peptide aggregates for 24 h at RT on a rotatory shaker. The samples were subsequently analyzed using confocal microscopy, which exhibited disaggregation of Aβ42 fibrils in the presence of RΔF NPs and SeNPs. However, complete fibril disappearance was found in the case of the fibrils co-incubated with RΔF-SeNPs (Fig. 5E)

3.12. Protective effects exhibited by NPs towards Aβ fibril-induced cytotoxicity

As amyloid aggregates display neurotoxic effects, the ability of RΔF-SeNPs to shield neuroblastoma cells from Aβ fibril-induced toxicity was determined *via* a live/dead staining assay. It was shown that SH-SY5Y cells represented a notable decline in their viability when being incubated with Aβ42 aggregates, while cell viability was restored to a great extent when the cells were co-incubated with RΔF-SeNPs and Aβ42 fibrils. However, this reduction in the cytotoxicity of fibrils towards SH SY5Y cells was not observed when Aβ fibrils were incubated with SeNPs (Fig. 5C). This was further confirmed *via* a resazurin assay (Fig. 5D). It was shown that SH-SY5Y cells depicted a decrease in their viability when being incubated with Aβ42 aggregates, while cell viability was regained when cells were co-incubated with RΔF-SeNPs and Aβ42 fibrils. However, this decrease in the cytotoxicity of fibrils towards SH SY5Y cells was not seen when Aβ fibrils were incubated with SeNPs as well as RΔF NP (Fig. 5C and 5D). Thus, our results demonstrated that RΔF-SeNPs were capable of shielding the neural cells from noxious Aβ42 peptide aggregates.

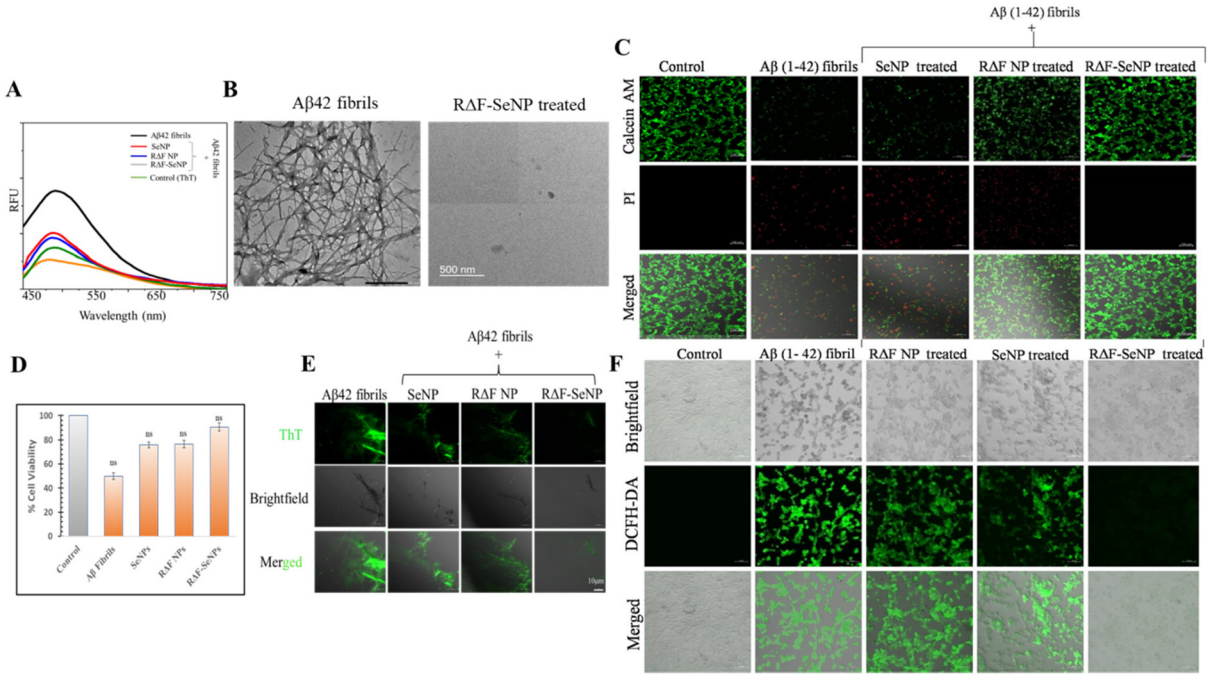

Fig. 5 Determination of the anti-aggregation effect exerted by different NPs on Aβ42 aggregates. (A) ThT aggregation kinetics of Aβ42 (at 5 μM) determined in the presence and absence of NPs. (B) TEM images depicting the complete loss of Aβ42 fibrils in the presence of RΔF-SeNPs. RΔF-SeNPs attenuated the aggregation process of Aβ42 fibrils (scale bar is 500 nm). (C) Confocal microscopic images of calcein AM/PI-stained cells depicting the shielding effects of SeNPs, RΔF NPs, and RΔF-SeNPs against Aβ42 fibril-generated cytotoxicity in SH-SY5Y cells (scale bar ~100 μm). (D) Quantitative data depicting the protective effect of SeNPs, RΔF NPs, and RΔF-SeNPs against Aβ42 fibril-induced cytotoxicity in SH-SY5Y cells analyzed *via* resazurin assay. (E) Fluorescence microscopic images of ThT-stained mature Aβ42 fibrils alone or incubated with SeNPs, RΔF NPs, and RΔF-SeNPs. Aβ42 fibrils incubated with RΔF-SeNPs depicted a complete loss of fluorescence intensity indicating a loss of the fibrillar aggregates. The scale bar is 10 μm. (F) Images showing the generation of an Aβ42 fibril-induced ROS response in SH-SY5Y cells with or without SeNPs, RΔF NPs, and RΔF-SeNPs (scale bar 50 μm).

3.13. Determination of the capability of NPs to reduce ROS production in SH-SY5Y cells induced by Aβ fibrils

Aβ fibrils are known to stimulate neuronal cell death *via* the formation of ROS. We accordingly hypothesized that RΔF-SeNPs would help mitigate neuronal toxicity and abrogate neuronal cell death *via* their antioxidant and anti-aggregation traits. To prove our hypothesis, we next examined the intracellular ROS-generation ability of amyloid fibrils in SH-SY5Y cells, both in the presence as well as the absence of the NPs, by carrying out a DCFH-DA assay. This assay enables the assessment of intracellular ROS levels by permitting the cellular uptake of a non-fluorescent probe (DCFH-DA), which is consequently hydrolyzed *via* intracellular esterase to produce dichlorofluorescein (DCFH).[81] We found that Aβ42 fibril-treated cells established a higher green fluorescence intensity for the cells co-treated with Aβ42 fibrils along with RΔF-SeNPs or SeNPs or RΔF NPs (Fig. 5F). Cells treated with both RΔF-SeNPs and Aβ42 fibrils simultaneously exhibited negligible intracellular green fluorescence, which can be correlated with the down-regulation of Aβ42 fibril-induced intracellular ROS levels in these cells by RΔF-SeNPs. However, cells treated with Aβ42 fibrils and RΔF NPs simultaneously showed a comparatively higher amount of Aβ-induced cellular ROS levels as compared with those incubated either with RΔF-SeNPs or SeNPs. Furthermore, these data indicated that RΔF-SeNPs were highly efficient at transforming Aβ fibrils into non-specific structures that induced fewer ROS in the SH-SY5Y cells.

3.14. Determination of the protective effects of NPs against FF and Ac-PHF6 oligomers

We have now explored the anti-amyloidogenic activity of RΔF-SeNPs towards both FF and Ac-PHF6 oligomers. Many previous studies have reported that the pre-fibrillar amyloid aggregates (soluble oligomers and protofibrils) of the causative amyloidogenic proteins such as tau protein, Aβ42 and α-synuclein display greater toxicity than the corresponding mature fibrils.[82,83] So, we also tried to obtain smaller oligomers of FF and Ac-PHF6 by sonicating the pre-formed fibrils of the peptides for 30 minutes, as mentioned earlier in the literature.[84] The oligomeric peptide aggregates obtained after sonication of the peptide were subsequently observed under AFM and a light microscope. We observed the formation of smaller protofibrillar and small globular structures as shown in Fig. 6A. We also observed that FF oligomeric species co-incubated with the NPs demonstrated distortion in the oligomeric structure. Our results depicted that the dislodging potential of RΔF-SeNPs towards FF oligomers was higher than those of

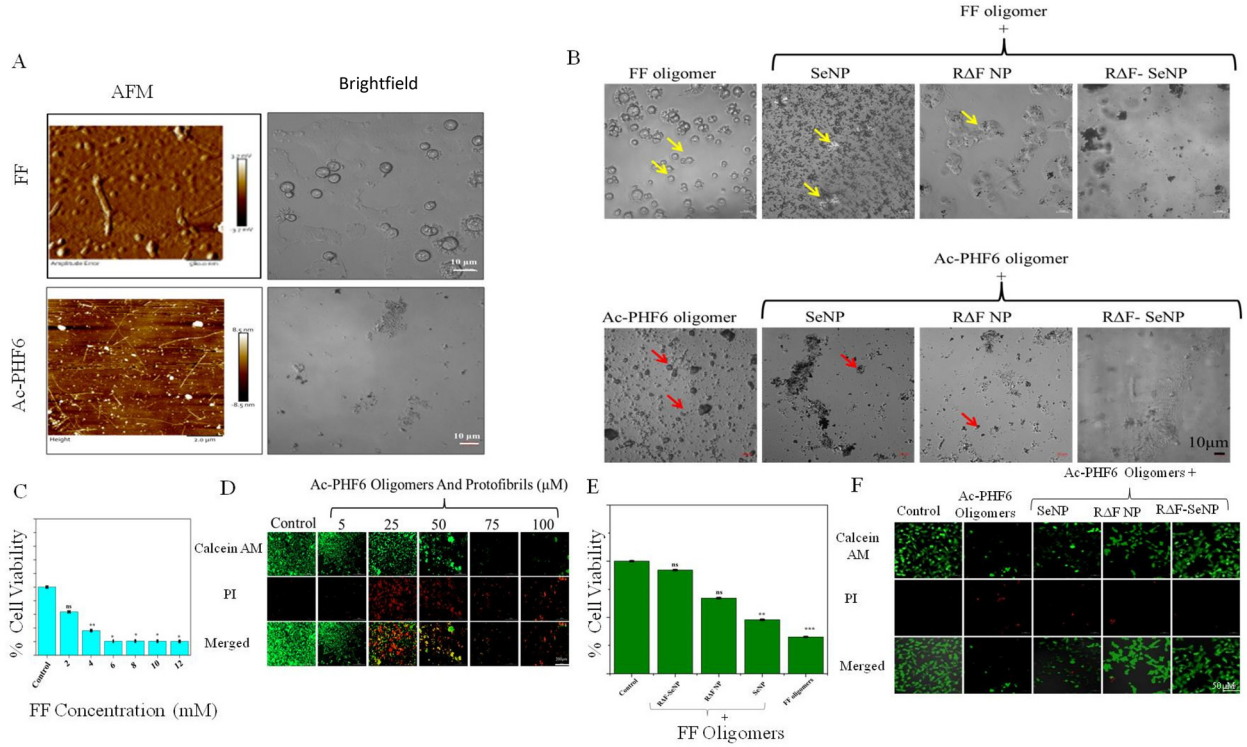

Fig. 6 (A) AFM and brightfield images demonstrating FF oligomers and Ac-PHF6 oligomers. (B) Microscopic images depicting the disruption of the FF and Ac-PHF6 oligomers by NPs. (C) Effect of FF oligomers on the viability of neuroblastoma SH-SY5Y cells, as examined using an MTT assay. (D) Fluorescence images of SHSY-5Y cells exposed to Ac-PHF6. Scale bar represents 200 μm. Green and red cells correspond to live cells (calcein-AM staining) and dead cells (PI staining), respectively. (E) The protective role played by SeNPs, RΔF NPs, and RΔF-SeNPs against FF oligomer-induced cytotoxicity in SH-SY5Y cells. (F) Live/dead cell viability images of cells captured following treatment with SeNPs, RΔF NPs, and RΔF-SeNPs in the presence of Ac-PHF6 oligomers (scale bar ~50 μm). The green color of the cells corresponds to live cells and the red color of the cells depicts dead cells.

SeNPS and RΔF NPs (Fig. 6B). Similarly, the Ac-PHF6 oligomer-dislodging potency of our NPs was carried out and results revealed that RΔF-SeNPs could efficiently distort Ac-PHF6 oligomers (Fig. 6B).

Many reports reveal that the oligomeric species formed by the aggregation of various amyloidogenic peptides could elicit cytotoxicity toward neuronal cells in a concentration-dependent manner. We also found that FF and Ac-PHF6 oligomers/short fibrils elicited toxicity toward SH-SY5Y cells in a concentration-dependent way. With respect to the untreated control, a 70% reduction in viable cells was observed in the case of cells that were treated with 6 mM of FF oligomers and 75 μM of Ac-PHF6 oligomers (Fig. 6C and D), respectively. We next continued to explore if RΔF-SeNPs could protect SH-SY5Y cells from FF oligomer-induced cell toxicity. SH-SY5Y cells were co-treated with FF oligomer (6 mM) and RΔF-SeNPs simultaneously for 24 h and their viability rate was assessed by an MTT assay. It was observed that the treatment of SH-SY5Y cells with FF oligomers and RΔF-SeNPs simultaneously displayed an extensive decrease in FF-induced cytotoxic effects. In this condition, cell viability was again restored to around 90% after a co-treatment duration of 24 h, signifying that RΔF-SeNPS can exert protective effects in FF oligomer-induced cytotoxicity (Fig. 6E).

Similarly, we further continued to explore the protective effect exerted by the NPs against Ac-PHF6 (75 μM) oligomer-induced cytotoxicity in SH-SY5Y cells. For this, cells were incubated with Ac-PHF6 oligomers with or without NPs for 24 h at 37 °C, followed by evaluating the cellular survival by a fluorescence (calcein AM/PI) assay. It was observed that, on incubating the cells with Ac-PHF6 oligomers (75 μM) alone, a 70% reduction in their cellular viability relative to the control cells was observed. The cells that were co-incubated with bare SeNPs also exhibited some red fluorescence along with the presence of viable green-fluorescent cells. RΔF NP-treated cells exhibited less red fluorescence, whereas RΔF-SeNPs treated cells expressed negligible red fluorescence. This verified that RΔF-SeNPs were able to protect the SH-SY5Y cells from the oligomer-induced cytotoxicity. Comparatively, SeNPs and RΔF NPs were less effective in rescuing cells from Ac-PHF6 fibril-induced cytotoxicity, as demonstrated in Fig. 6F.

3.15. Validation of streptozotocin (STZ)-induced cytotoxicity in neuronal N2a cells

It has been shown that the intra-cerebroventricular (ICV) administration of STZ into the brain of rats leads to memory loss, enhanced oxidative stress, and cell death in AD.[85] Rodents administered with STZ *via* the ICV mode are a well-

established model of dementia.[39] STZ is also utilized to investigate and decipher the cellular mechanisms that may lead to the death of neurons in AD. Various studies have reported that STZ exerts cytotoxicity on different neural cell types.[86–88] STZ-treated N2a cells have been reported as *in vitro* experimental test models for AD. STZ-induced neurotoxicity at the cellular and molecular levels has been shown to involve AD-associated pathological markers.[37] Thus, on this basis, we used STZ-treated N2a cells as a model to authenticate the anti-amyloidogenic properties of the NPs. As reported earlier, STZ demonstrated a concentration-dependent cytotoxicity toward N2a cells as validated by an MTT assay (Fig. 7A).

3.15.1. Determination of the neuroprotective effects exhibited by NPs toward STZ-induced cytotoxicity in N2a cells. We next tried to decipher the protective effect of the NPs on STZ-treated cells. In addition to exhibiting suitable efficacy, it is important that the target nanoparticulate systems should gain successful entry into the cells. Thus, we first tried to understand the cellular uptake behavior of the systems in the N2a cells. For this purpose, cells were first incubated with rhoda-

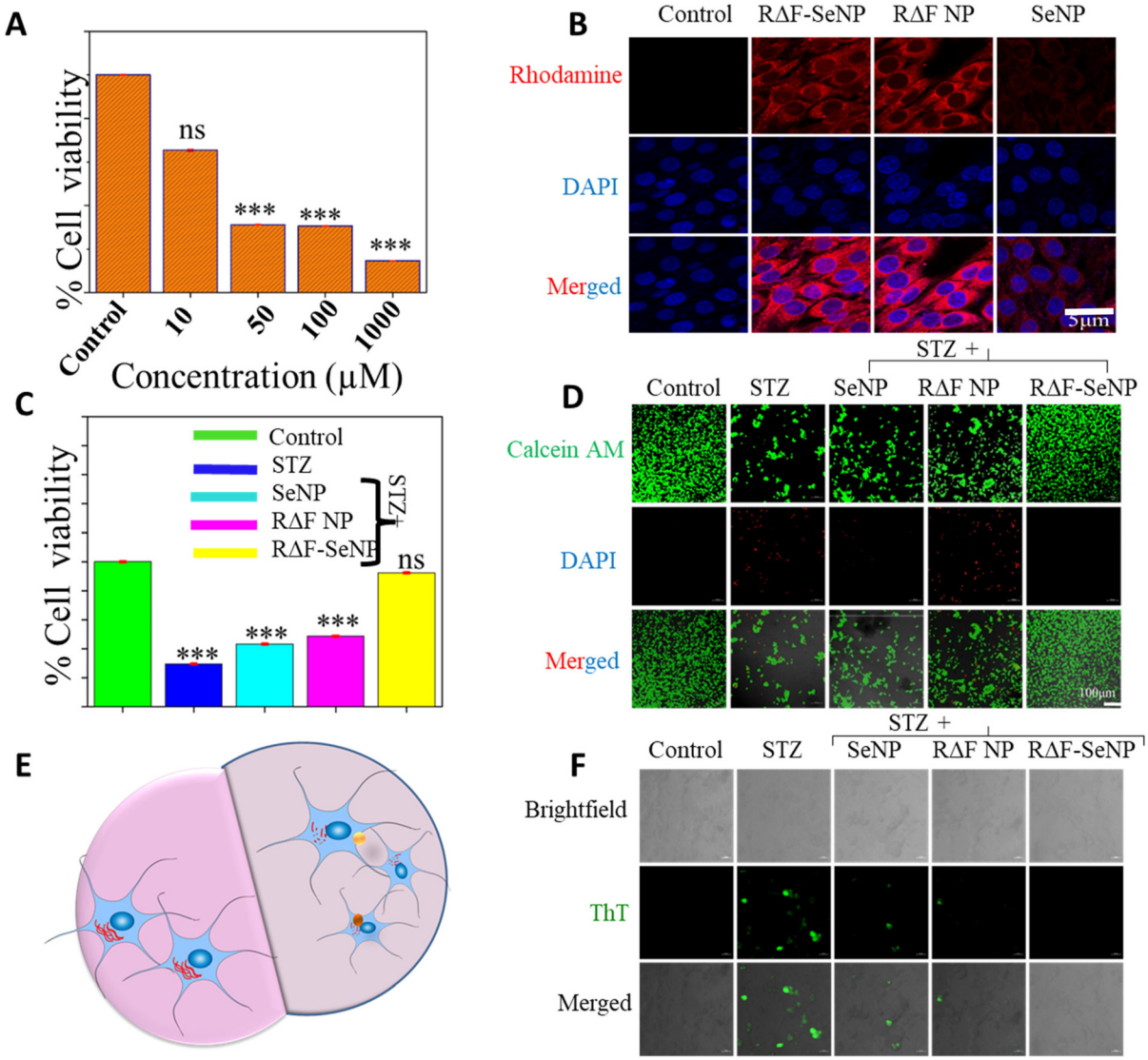

Fig. 7 (A) STZ-induced cytotoxicity in mouse neuronal N2a cells assessed *via* an MTT assay. (B) Cellular uptake study results depicting the internalization of NPs inside N2a cells. (C) Protective effects exhibited by NPs in STZ-induced cytotoxicity in N2a cells. (D) Microscopic images of calcein AM/PI pre-stained cells depicting the shielding effects of the SeNPs, RΔF NPs, and RΔF-SeNPs against STZ-prompted cytotoxicity in N2a cells (scale bar ~100 μm). Green fluorescence of the cells corresponds to viable cells whereas red fluorescence of the cells correlates to non-viable cells. (E) Schematic illustration demonstrating the protective effect of RΔF-SeNPs exhibited in STZ-treated N2a cells. (F) Amyloid aggregation in neuronal N2a cells as illustrated by a ThT staining assay in STZ and STZ + NPs treated N2a cells. The data are represented as mean ± SD. Statistical analysis was carried out using a Kruskal–Wallis test followed by a Dunn's multiple comparison test. Significance levels are expressed as * $p < 0.05$; ** $p < 0.01$; *** $p < 0.001$, ns is non-significant.

mine 6G-labeled RΔF-SeNPs, RΔF, and SeNPs, for a duration of 24 h followed by imaging under a confocal microscope. Within 24 h, a feeble intra-cellular fluorescence was observed in the case of bare SeNP-treated cells, suggesting their low intracellular uptake into the N2a cells. However, RΔF NP-treated cells exhibited high fluorescence intensity, suggesting their greater internalization in N2a cells. However, in the case of RΔF-SeNP-treated cells, a drastically enhanced fluorescence intensity was observed in the cytoplasm and the nucleus, indicating that the RΔF-SeNPs attained the maximum cellular uptake inside the neural cells due to their smaller size (Fig. 7B)

We next continued to explore if RΔF-SeNPs could rescue N2a cells from STZ-induced cytotoxicity. For this study, N2a cells were treated with STZ and NPs at 37 °C for 48 h, and cellular viability was assessed by an MTT assay. Furthermore, the study outcome depicted that the incubation of N2a cells with STZ alone decreased their viability in a concentration-dependent manner, whereas N2a cells co-incubated with RΔF-SeNPs arrayed a notable decline in the STZ-induced cytotoxic effects. In this, the viable cells were restored to roughly 95% after a co-treatment period of 48 h, representing that RΔF-SeNPs were able to shield cells from the cytotoxicity caused by the STZ, as shown in Fig. 7C. Moreover, these data were further supported by microscopic analysis (Fig. S12†) where a protective effect of RΔF-SeNPs towards STZ-treated N2a cells was evident. To further add to the colorimetric MTT assay, a live/dead cell viability examination was carried out. The results of the assay illustrated that STZ alone (1000 μM) demonstrated a large amount of red-fluorescent cells, signifying its cytotoxic behavior. Cells co-incubated along with STZ and bare SeNPs also exhibited some red fluorescence along with the presence of viable green-fluorescing cells. RΔF NP-treated cells exhibited less red fluorescence, whereas RΔF-SeNP-treated cells expressed negligible red fluorescence. Thus, the higher green fluorescence exerted by the cells incubated with RΔF-SeNPs confirmed their neuroprotective effects ((Fig. 7D and 7E) Amyloid protein aggregation is one of the foremost emblems of AD. To further explore and validate STZ-induced amyloidogenic protein aggregation inside N2a cells, we carried out an intracellular fluorescence-based ThT assay in cells treated with STZ alone or in cells treated with both STZ along with either RΔF NPs or SeNPs or RΔF-SeNPs. As shown in Fig. 7F a large amount of amyloid protein aggregation was observed in the cells treated with STZ. When the neural cells were co-incubated with STZ and RΔF NPs or SeNPs, a marginal reduction in the ThT fluorescence intensity was observed. Conversely, in the presence of RΔF-SeNPs, there was an absolute decline in the intracellular ThT fluorescence. All together, these results indicated that both RΔF NPs and SeNPs were less effective against ceasing STZ-induced amyloid aggregation in N2a cells. However, RΔF-SeNPs could efficiently inhibit amyloid protein aggregation in STZ-treated N2a cells. We hypothesized that the increased cellular uptake of RΔF-SeNPs could account for their enhanced ability to inhibit amyloid protein aggregation in N2a cells.

3.16. Determination of the ability of NPs to cross the BBB

The BBB is a safeguard system that shields the brain from detrimental products and prevents anti-AD entities from entering the brain. We, therefore, examined the ability of RΔF-SeNPs to pass through the BBB using ICP-MS. ICP-MS depicted that the animals treated with RΔF-SeNPs (approximately 11.79 ppm) had a higher concentration of Se in their brain compared with the controls (approximately 0.51 ppm). Encouraged by these results we performed fluorescence *in vivo* imaging assay of ICG-labelled NPs in mice to determine their ability to reach

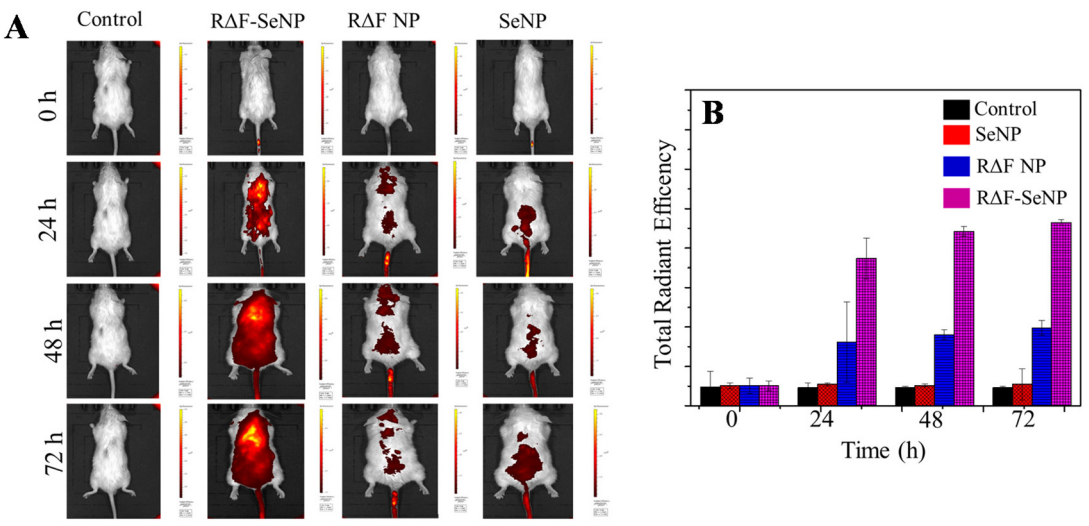

Fig. 8 *In vivo* fluorescence images of dye-labeled NPs obtained in Balb/c mice. (A) *In vivo* fluorescence images of mice captured after 0, 24, 48, and 72 h of nanoparticle administration. (B) Semiquantitative fluorescence assessment in the brain region of mice captured at different time intervals after administering the animals with SeNPs, RΔF NPs, and RΔF-SeNPs. Results revealed that RΔF-SeNPs could successfully reach the brain tissues and be retained there, thus serving as a brain drug-delivery agent.

the brain tissues. Fluorescence images of the mice administered with NPs were taken at different time points, utilizing IVIS. As revealed in Fig. 8 (A and B), the fluorescent signals in the brain areas of RΔF-SeNP-treated mice amplified progressively over time, depicting the efficient passage of RΔF-SeNPs across the BBB to reach the brain tissues. RΔF NPs could also reach the brain tissues and stayed there for a significant period, as evident from the IVIS images of the animals. However, in the case of the only-SeNP-treated group, no increased fluorescent signal was seen in the brain region of the treated animals, confirming their inability to cross through the barrier. Thus, the passage of RΔF-SeNPs across the BBB could be attributed to their RΔF NP coating as bare SeNPs did not exhibit any transport ability across the BBB to get into the brain tissues.

3.17. *In vivo* assessment of RΔF-SeNP efficacy in the ICV-STZ-induced AD rat model

3.17.1. Cognitive impairment exhibited by RΔF-SeNPs in the ICV-STZ-induced rat model. We next investigated whether RΔF-SeNPs ameliorated the long-term memory in STZ-treated rats. For the assay, CSF/STZ-injected rats were trained in the Morris water maze to locate the hidden platform for three days. It was observed that STZ-lesioned rats exhibited significantly longer escape latency times to find the hidden platform. However, RΔF-SeNP treatment (STZ + RΔF-SeNPs) in the lesioned rats considerably improved their learning ability, and these rats exhibited appreciably lower escape latencies than STZ-treated rats. Spatial learning and memory (MWM) experiments were performed to understand the cognitive performance of the animals. Our results demonstrated that as the training time enhanced, the escape latency of animals in each group steadily decreased. Two-way ANOVA was utilized to evaluate the escape latency period. On the first day of the trial, there was no statistically noteworthy variation in the escape latency duration between the groups. However, the escape latency episode of rats treated with RΔF-SeNPs on days 2 and 3 was decreased significantly (Fig. 9A, $p < 0.0001$, $F(3, 58) = 237.8$) when compared with the STZ given on the same day. The space exploration time on days 2 and 3 after the RΔF-SeNP exposure gradually shortened (Fig. 9B, $p < 0.0001$, $F(3, 56) = 79.99$) and the target quadrant dwelling time (Fig. 9C, $p <$

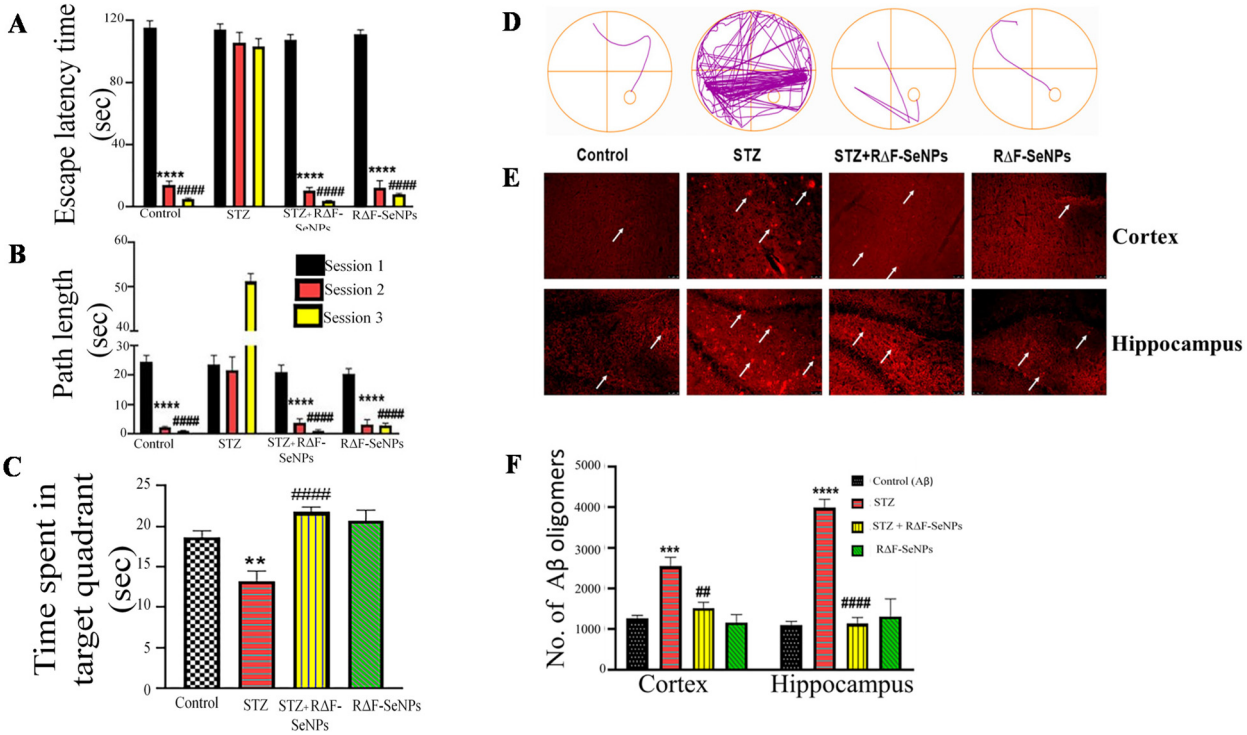

Fig. 9 RΔF-SeNP treatment (5 mg kg^{-1}, i.v.) improved memory and learning in STZ-lesioned animals. Spatial memory and learning functions were determined by the Morris water maze test. (A) The bar graph illustrating the escape latency time (in s), *i.e.*, the time taken to arrive at the hidden podium by the animals. (B) The graph depicts the mean path length (in cm) traveled by the animals. (C) The time spent in the target quadrant by the animals in each group. (D) Representative track plots for the path traced by a rat of each group. The data are explained as mean ± SEM of $n = 6$ rats per group. Data were studied by repeated-measures two-way ANOVA, followed by the Bonferroni *post hoc* test. Values are mean ± SEM, $n = 6$. *$p <$ 0.05, **$p < 0.01$, ***$p < 0.001$. #$p < 0.05$, ##$p < 0.01$, ###$p < 0.001$. * Session 1 *vs.* session 3, # session 1 *vs.* session 2. * control *vs.* STZ, # STZ *vs.* STZ + RΔF-SeNPs. (E) Representative photomicrograph depicting immunostaining of Aβ42 oligomers in both the cortex and the hippocampus. (F) RΔF-SeNP treatment subsided the expression of Aβ42 protein in the cortex as well as the hippocampus. Data were assessed through two-way ANOVA, followed by a Bonferroni multiple comparison test (*$P < 0.05$, **$P < 0.01$, ***$P < 0.001$; ****$P < 0.0001$; #$P < 0.05$, ##$P < 0.01$, ###$P < 0.001$; ####$P < 0.0001$). *Control *vs.* STZ; #STZ *vs.* STZ + RΔF-SeNPs.

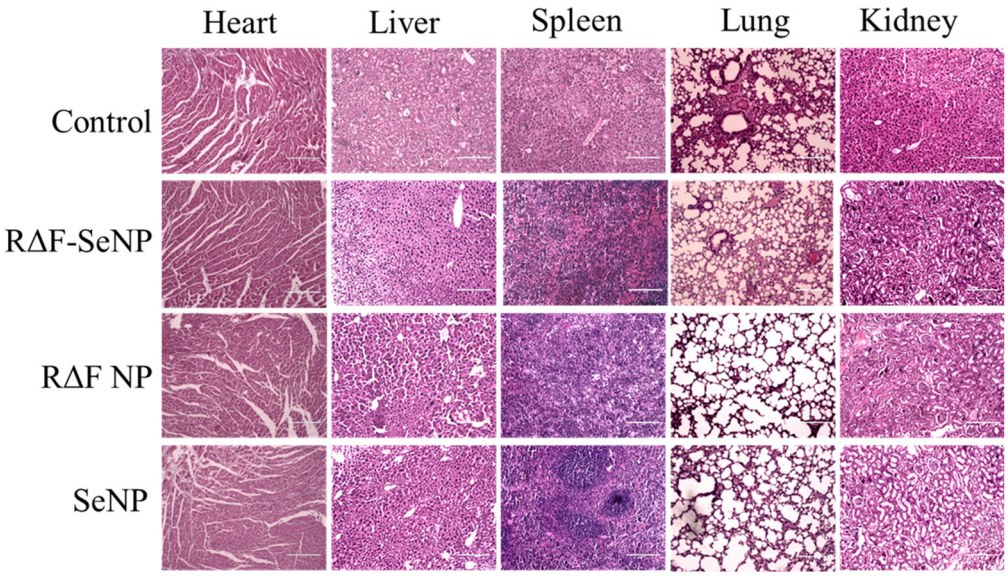

Fig. 10 H&E staining images of lungs, hearts, spleens, livers, and kidneys obtained 72 h post administration of NPs (RΔF-SeNPs, RΔF NPs and SeNPs) (scale bar 200 μm). The images showed no morphological alterations in the tissue samples after NP administration.

0.0001, $F(3, 20) = 12.87$) of rats was enhanced as compared with STZ-alone-treated rats. Fig. 9D depicts the swimming trajectory. Afterward, with an increase in training days, the swimming path of rats in the control and RΔF-SeNP-treated groups became clearer as they reached the display place persistently, whereas the rats in the STZ-exposed group could hardly reach the podium and their swimming trajectories were confused and unsystematic. The results of the water maze suggested that RΔF-SeNP exposure was able to prevent impairment in the learning and memory function of rats.

3.17.2. Neuroprotection exerted by RΔF-SeNPs against Aβ burden in the ICV-STZ-lesioned AD rats. In this study, we also examined the cortical and hippocampal Aβ load after RΔF-SeNP treatment in STZ-lesioned rats (Fig. 9E and F). The levels of Aβ42 in the cortex, as well as hippocampus, significantly improved between the groups after RΔF-SeNP treatment (Fig. 9E, $F(1, 32) = 2.951$). The ICV-STZ-injected rats showed significantly higher levels of Aβ42 aggregates in the cortex and hippocampus than the aCSF-treated rats. Conversely, RΔF-SeNP-treated rats had a reduced percentage of Aβ oligomers in the neurons of the cortex ($p < 0.001$) and hippocampus ($p < 0.0001$) regions than those of the STZ-lesioned rats. Furthermore, the administration of RΔF-SeNPs to control rats without any AD-like symptoms presented similar cognitive behavioral results as that of the control.

3.17.3. Effect of RΔF-SeNPs on the body weight of rats. Before the intervention, the observed body weight of rats in the control group was 229.83 ± 11.51 g. In the ICV-STZ-injected group, it was 190.17 ± 5.61 g. In the ICV STZ + RΔF-SeNP-treated group the observed body weight was 206.33 ± 4.56 g and in the RΔF-SeNP (*prse*) group it was 218.67 ± 5.09 g. After the intervention, the body weight of the rats in the control group was found to be 278.17 ± 14.72 g. In the ICV-STZ-lesioned group it was 281.83 ± 13.38 g. In the ICV STZ + RΔF-SeNP-treated group it was 248.33 ± 8.78 g, and in the RΔF-SeNP (*prse*) group it was 295.33 ± 14.72 g. During the intervention, no significant negative impact on the body weight of rats was observed in the control (aCSF), ICV STZ, ICV STZ + RΔF-SeNPs, and RΔF-SeNP groups (Fig. S13†).

3.18. Biosafety of NPs *in vivo*

To assess the biosafety of NPs *in vivo*, hematoxylin and eosin (H&E) staining of organs (heart, spleen, liver, lung, and kidneys) extracted from mice was performed. The histological examination showed that the organs of mice treated with NPs (RΔF-SeNPs, RΔF NPs and SeNPs) retained their complete structure and no pathological changes were observed. This indicated that NPs were biocompatible and exhibited no toxicity *in vivo.* Thus, these are safe to use under the current dose (Fig. 10).

4. Conclusion

Amyloid and tau pathologies are considered to be the pivotal pathogenic factors responsible for AD onset as well as progression, and therefore are potential targets for many disease-modifying drugs aiming to attain a cure for the disease. Therefore, in our study, we focused on the development of new multifunctional RΔF-SeNPs with potential fibril-disaggregating potencies for three different peptide-based amyloidogenic models. In this study, FF and Ac-PHF6 were used as reductionist models to explore the anti-amyloidogenic activity of our peptide–metal hybrid nanostructures, RΔF-SeNPs. Interestingly, the as-synthesized RΔF-SeNPs were capable of disaggregating amyloidogenic fibrils formed by the dipeptide

FF, the hexapeptide Ac-PHF6 as well as the full-length protein Aβ42. In addition, it was observed that FF and Ac-PHF6 fibrils caused toxicity to SH-SY5Y cells. Conversely when these were co-incubated with the RΔF-SeNPs, cell death was drastically reduced. Additionally, we also tested the anti-amyloidogenic potency of our nanosystems in STZ-treated neuronal N2a cells chosen as an *in vitro* experimental model for the disease. We found that RΔF-SeNPs exhibited protective effects toward the STZ-treated N2a cells and decreased the amount of amyloid protein aggregation in STZ-treated N2a cells, as evidenced by the ThT fluorescence assay. Fluorescent signals in the brain areas of RΔF-SeNP-treated mice increased progressively in due course, pointing toward a successful BBB-breaching ability of RΔF-SeNPs. We moreover observed an improved neuroprotective effect of RΔF-SeNPs in memory and spatial learning in the STZ-induced rat model of AD. Additionally, RΔF-SeNPs reduced Aβ42 deposition in the cortex and hippocampus areas of the brain tissues in AD model rats. Thus, our research findings provide insights into the fabrication of a novel form of SeNPs which would serve as a neuroprotective entity with a wide application prospect in the research of identifying novel disease-modifying AD drugs.

Conflicts of interest

There are no conflicts to declare.

Acknowledgements

J. J. P. thanks SERB-POWER (SPG/2021/002910) grant, CSIR-grant (37/1755/23/EMR-I), DBT-Har Gobind Khorana-Innovative Young Biotechnologist (BT/13//IYBA/2020/08) and DBT grant (BT/PR36632/NNT/28/1694/2020) for partial funding. A. K. thanks ICMR, India for the fellowship.

References

1 S. Tiwari, V. Atluri, A. Kaushik, A. Yndart and M. Nair, *Int. J. Nanomed.*, 2019, **14**, 5541.
2 R. Tarawneh and D. M. Holtzman, *Cold Spring Harbor Perspect. Med.*, 2012, **2**, a006148.
3 Alzheimer's Disease Facts and Figures, **https://www.alz.org/alzheimers-dementia/facts-figures**, (accessed March 26, 2023).
4 L. M. Ittner and J. Götz, *Nat. Rev. Neurosci.*, 2011, **12**, 67–72.
5 U. Tinggi, *Environ. Health Prev. Med.*, 2008, **13**, 102–108.
6 F. P. Bellinger, A. V. Raman, M. A. Reeves and M. J. Berry, *Biochem. J.*, 2009, **422**, 11–22.
7 D. Vicente-Zurdo, I. Romero-Sánchez, N. Rosales-Conrado, M. E. León-González and Y. Madrid, *Anal. Bioanal. Chem.*, 2020, **412**, 6485–6497.
8 G. L. Godoi, L. de Oliveira Porciúncula, J. F. Schulz, F. N. Kaufmann, J. B. Da Rocha, D. O. G. de Souza, G. Ghisleni and H. L. de Almeida, *Neurochem. Res.*, 2013, **38**, 2359–2363.
9 J. Wang, P. Um, B. A. Dickerman and J. Liu, *Nutrients*, 2018, **10**, 584.
10 R. F. Burk, K. E. Hill, A. K. Motley, V. P. Winfrey, S. Kurokawa, S. L. Mitchell and W. Zhang, *FASEB J.*, 2014, **28**, 3579.
11 A. Van der Jeugd, A. Parra-Damas, R. Baeta-Corral, C. M. Soto-Faguás, T. Ahmed, F. M. LaFerla, L. Giménez-Llort, R. D'Hooge and C. A. Saura, *Sci. Rep.*, 2018, **8**, 6431.
12 B. Hosnedlova, M. Kepinska, S. Skalickova, C. Fernandez, B. Ruttkay-Nedecky, Q. Peng, M. Baron, M. Melcova, R. Opatrilova and J. Zidkova, *Int. J. Nanomed.*, 2018, 2107–2128.
13 W.-Y. Tzeng, Y.-H. Tseng, T.-T. Yeh, C.-M. Tu, R. Sankar, Y.-H. Chen, B.-H. Huang, F.-C. Chou and C.-W. Luo, *Opt. Express*, 2020, **28**, 685–694.
14 T. Nie, H. Wu, K.-H. Wong and T. Chen, *J. Mater. Chem. B*, 2016, **4**, 2351–2358.
15 N. Srivastava and M. Mukhopadhyay, *Powder Technol.*, 2013, **244**, 26–29.
16 Z. Lin, Y. Li, M. Guo, M. Xiao, C. Wang, M. Zhao, T. Xu, Y. Xia and B. Zhu, *RSC Adv.*, 2017, **7**, 35290–35296.
17 L. Rao, Y. Ma, M. Zhuang, T. Luo, Y. Wang and A. Hong, *Int. J. Nanomed.*, 2014, **9**, 4819.
18 T. Huang, J. A. Holden, E. C. Reynolds, D. E. Heath, N. M. O'Brien-Simpson and A. J. O'Connor, *ACS Appl. Mater. Interfaces*, 2020, **12**, 55696–55709.
19 F. Yang, Q. Tang, X. Zhong, Y. Bai, T. Chen, Y. Zhang, Y. Li and W. Zheng, *Int. J. Nanomed.*, 2012, 835–844.
20 H. Amani, R. Habibey, F. Shokri, S. J. Hajmiresmail, O. Akhavan, A. Mashaghi and H. Pazoki-Toroudi, *Sci. Rep.*, 2019, **9**, 6044.
21 S. Rajeshkumar, L. Ganesh and J. Santhoshkumar, *Nanobiotechnology in Neurodegenerative Diseases*, 2019, pp. 209–224.
22 Y. Gong, A. Huang, X. Guo, Z. Jia, X. Chen, X. Zhu, Y. Xia, J. Liu, Y. Xu and X. Qin, *Chem. Eng. J.*, 2021, **418**, 129345.
23 J. Sun, C. Wei, Y. Liu, W. Xie, M. Xu, H. Zhou and J. Liu, *Biomaterials*, 2019, **197**, 417–431.
24 T. Yin, L. Yang, Y. Liu, X. Zhou, J. Sun and J. Liu, *Acta Biomater.*, 2015, **25**, 172–183.
25 L. Yang, Y. Cui, H. Liang, Z. Li, N. Wang, Y. Wang and G. Zheng, *ACS Appl. Mater. Interfaces*, 2022, **14**, 30557–30570.
26 M. Chen, Y. Huang, X. Zhu, X. Hu and T. Chen, *Adv. Ther.*, 2018, **1**, 1800074.
27 C. D. Arvanitis, G. B. Ferraro and R. K. Jain, *Nat. Rev. Cancer*, 2020, **20**, 26–41.
28 D. B. Teplow, *Methods Enzymol.*, 2006, **413**, 20–33.
29 K. Tenidis, M. Waldner, J. Bernhagen, W. Fischle, M. Bergmann, M. Weber, M.-L. Merkle, W. Voelter, H. Brunner and A. Kapurniotu, *J. Mol. Biol.*, 2000, **295**, 1055–1071.
30 M. Reches, Y. Porat and E. Gazit, *J. Biol. Chem.*, 2002, **277**, 35475–35480.

31 V. Castelletto, P. Ryumin, R. Cramer, I. W. Hamley, M. Taylor, D. Allsop, M. Reza, J. Ruokolainen, T. Arnold and D. Hermida-Merino, *Sci. Rep.*, 2017, **7**, 43637.
32 E. Gazit, *FEBS J.*, 2005, **272**, 5971–5978.
33 S. Brahmachari, Z. A. Arnon, A. Frydman-Marom, E. Gazit and L. Adler-Abramovich, *ACS Nano*, 2017, **11**, 5960–5969.
34 A. Kour, T. Dube, A. Kumar and J. J. Panda, *Bioconjugate Chem.*, 2022, **33**, 397–410.
35 M. von Bergen, P. Friedhoff, J. Biernat, J. Heberle, E.-M. Mandelkow and E. Mandelkow, *Proc. Natl. Acad. Sci.*, 2000, **97**, 5129–5134.
36 M. Von Bergen, S. Barghorn, L. Li, A. Marx, J. Biernat, E.-M. Mandelkow and E. Mandelkow, *J. Biol. Chem.*, 2001, **276**, 48165–48174.
37 M. Frenkel-Pinter, S. Tal, R. Scherzer-Attali, M. Abu-Hussien, I. Alyagor, T. Eisenbaum, E. Gazit and D. Segal, *Neurodegener. Dis.*, 2017, **17**, 73–82.
38 G. K. Viswanathan, A. Paul, E. Gazit and D. Segal, *Front. Cell Dev. Biol.*, 2019, **7**, 242.
39 H. Lannert and S. Hoyer, *Behav. Neurosci.*, 1998, **112**, 1199.
40 E. E. Genrikhs, E. V. Stelmashook, S. A. Golyshev, O. P. Aleksandrova and N. K. Isaev, *Brain Res. Bull.*, 2017, **130**, 90–94.
41 J. Biswas, P. Goswami, S. Gupta, N. Joshi, C. Nath and S. Singh, *Mol. Neurobiol.*, 2016, **53**, 2794–2806.
42 J. J. Panda, A. Kaul, S. Kumar, S. Alam, A. K. Mishra, G. C. Kundu and V. S. Chauhan, *Nanomedicine*, 2013, **8**, 1927–1942.
43 S. Alam, J. J. Panda, T. K. Mukherjee and V. S. Chauhan, *J. Nanobiotechnol.*, 2016, **14**, 1–14.
44 P. K. Singh, S. Chibh, T. Dube, V. S. Chauhan and J. J. Panda, *Pharm. Res.*, 2018, **35**, 1–11.
45 A. M. Fanni, C. M. Vander Zanden, P. V. Majewska, J. Majewski and E. Y. Chi, *J. Biol. Chem.*, 2019, **294**, 15304–15317.
46 J. Zhang, X. Zhou, Q. Yu, L. Yang, D. Sun, Y. Zhou and J. Liu, *ACS Appl. Mater. Interfaces*, 2014, **6**, 8475–8487.
47 M. I. Sulatsky, A. I. Sulatskaya, O. I. Povarova, I. A. Antifeeva, I. M. Kuznetsova and K. K. Turoverov, *Prion*, 2020, **14**, 67–75.
48 D. Vicente-Zurdo, S. Rodríguez-Blázquez, E. Gómez-Mejía, N. Rosales-Conrado, M. E. León-González and Y. Madrid, *Anal. Bioanal. Chem.*, 2022, **414**, 7573–7584.
49 S. K. Mishra, S. Singh, S. Shukla and R. Shukla, *Neurochem. Int.*, 2018, **113**, 56–68.
50 S. Singh, A. Mishra, S. Bharti, V. Tiwari, J. Singh and S. Shukla, *Mol. Neurobiol.*, 2018, **55**, 6500–6517.
51 Y. Feng, J. Su, Z. Zhao, W. Zheng, H. Wu, Y. Zhang and T. Chen, *Dalton Trans.*, 2014, **43**, 1854–1861.
52 M. Vahdati and T. Tohidi Moghadam, *Sci. Rep.*, 2020, **10**, 510.
53 B. Smith, *Spectroscopy*, 2018, **33**, 24–29.
54 R. Khurana, C. Coleman, C. Ionescu-Zanetti, S. A. Carter, V. Krishna, R. K. Grover, R. Roy and S. Singh, *J. Struct. Biol.*, 2005, **151**, 229–238.
55 Y. Pang, Q. Zhang, X. Sun, J. Ji, F. Pi and X. Shen, *Int. J. Electrochem. Sci.*, 2018, **13**, 8518–8529.
56 P. C. Ke, E. H. Pilkington, Y. Sun, I. Javed, A. Kakinen, G. Peng, F. Ding and T. P. Davis, *Adv. Mater.*, 2020, **32**, 1901690.
57 C. Cabaleiro-Lago, F. Quinlan-Pluck, I. Lynch, S. Lindman, A. M. Minogue, E. Thulin, D. M. Walsh, K. A. Dawson and S. Linse, *J. Am. Chem. Soc.*, 2008, **130**, 15437–15443.
58 G. R. Lamberto, A. Binolfi, M. L. Orcellet, C. W. Bertoncini, M. Zweckstetter, C. Griesinger and C. O. Fernández, *Proc. Natl. Acad. Sci. U. S. A.*, 2009, **106**, 21057–21062.
59 E. Gazit, *FASEB J.*, 2002, **16**, 77–83.
60 S. Brahmachari, A. Paul, D. Segal and E. Gazit, *Future Med. Chem.*, 2017, **9**, 797–810.
61 A. Franko, D. C. Rodriguez Camargo, A. Böddrich, D. Garg, A. Rodriguez Camargo, B. Rathkolb, D. Janik, M. Aichler, A. Feuchtinger and F. Neff, *Sci. Rep.*, 2018, **8**, 1116.
62 Y. Xu, Y. Zhang, Z. Quan, W. Wong, J. Guo, R. Zhang, Q. Yang, R. Dai, P. L. McGeer and H. Qing, *Neurochem. Res.*, 2016, **41**, 2788–2796.
63 A. Paul, G. K. Viswanathan, S. Mahapatra, G. Balboni, S. Pacifico, E. Gazit and D. Segal, *ACS Chem. Neurosci.*, 2019, **10**, 3510–3520.
64 S. S. Mamsa and B. P. Meloni, *Front. Mol. Neurosci.*, 2021, **14**, 759729.
65 T. Kawasaki, K. Onodera and S. Kamijo, *Biosci., Biotechnol., Biochem.*, 2011, **75**, 1496–1501.
66 T. Kawasaki and S. Kamijo, *Biosci., Biotechnol., Biochem.*, 2012, **76**, 762–766.
67 L. Yang, J. Sun, W. Xie, Y. Liu and J. Liu, *J. Mater. Chem. B*, 2017, **5**, 5954–5967.
68 K. Iqbal, F. Liu, C.-X. Gong and I. Grundke-Iqbal, *Curr. Alzheimer Res.*, 2010, **7**, 656–664.
69 A. Alonso, T. Zaidi, M. Novak, I. Grundke-Iqbal and K. Iqbal, *Proc. Natl. Acad. Sci. U. S. A.*, 2001, **98**, 6923–6928.
70 C. Ballatore, V. M.-Y. Lee and J. Q. Trojanowski, *Nat. Rev. Neurosci.*, 2007, **8**, 663–672.
71 N. Ghoshal, F. García-Sierra, J. Wuu, S. Leurgans, D. A. Bennett, R. W. Berry and L. I. Binder, *Exp. Neurol.*, 2002, **177**, 475–493.
72 A. W. P. Fitzpatrick, B. Falcon, S. He, A. G. Murzin, G. Murshudov, H. J. Garringer, R. A. Crowther, B. Ghetti, M. Goedert and S. H. W. Scheres, *Nature*, 2017, **547**, 185–190.
73 J. A. Plumley and J. J. Dannenberg, *J. Phys. Chem. B*, 2011, **115**, 10560–10566.
74 H. Inouye, D. Sharma, W. J. Goux and D. A. Kirschner, *Biophys. J.*, 2006, **90**, 1774–1789.
75 V. G. KrishnaKumar, A. Paul, E. Gazit and D. Segal, *Sci. Rep.*, 2018, **8**, 71.
76 H. Geng, Y. Pan, R. Zhang, D. Gao, Z. Wang, B. Li, N. Li, D. Guo and C. Xing, *Adv. Funct. Mater.*, 2021, **31**, 2102953.
77 C. Yan, N. Zhang, P. Guan, P. Chen, S. Ding, T. Hou, X. Hu, J. Wang and C. Wang, *Int. J. Biol. Macromol.*, 2020, **153**, 723–735.
78 N. Andrikopoulos, Z. Song, X. Wan, A. M. Douek, I. Javed, C. Fu, Y. Xing, F. Xin, Y. Li and A. Kakinen, *Chem. Mater.*, 2021, **33**, 6484–6500.
79 P. R. Bharadwaj, A. K. Dubey, C. L. Masters, R. N. Martins and I. G. Macreadie, *J. Cell. Mol. Med.*, 2009, **13**, 412–421.
80 P. Kumar, A. Nagarajan and P. D. Uchil, *Cold Spring Harb. Protoc.*, 2018, 462–464.

81 S. I. Dikalov and D. G. Harrison, *Antioxid. Redox Signal.*, 2014, **20**, 372–382.
82 P. C. Ke, R. Zhou, L. C. Serpell, R. Riek, T. P. Knowles, H. A. Lashuel, E. Gazit, I. W. Hamley, T. P. Davis and M. Fändrich, *Chem. Soc. Rev.*, 2020, **49**, 5473–5509.
83 M. Verma, A. Vats and V. Taneja, *Ann. Indian Acad. Neurol.*, 2015, **18**, 138.
84 A. M. Fanni, C. M. Vander Zanden, P. V. Majewska, J. Majewski and E. Y. Chi, *J. Biol. Chem.*, 2019, **294**, 15304–15317.
85 F. Bagaméry, K. Varga, K. Kecsmár, I. Vincze, É. Szökő and T. Tábi, *Neurochem. Res.*, 2021, **46**, 1350–1358.
86 N. K. Isaev, E. E. Genrikhs, D. N. Voronkov, M. R. Kapkaeva and E. V. Stelmashook, *Toxicol. Appl. Pharmacol.*, 2018, **348**, 99–104.
87 K. Plaschke and J. Kopitz, *J. Neural Transm.*, 2015, **122**, 551–557.
88 J. Park, J. Won, J. Seo, H.-G. Yeo, K. Kim, Y. G. Kim, C.-Y. Jeon, M. K. Kam, Y.-H. Kim, J.-W. Huh, S.-R. Lee, D.-S. Lee and Y. Lee, *Front. Cell. Neurosci.*, 2020, **14**, 235.